



Rh single atoms/clusters confined in metal sulfide/oxide nanotubes as advanced multifunctional catalysts for green and energy-saving hydrogen productions

Dinh Chuong Nguyen^a, Thi Luu Luyen Doan^a, Sampath Prabhakaran^a, Do Hwan Kim^b, Nam Hoon Kim^{a,*}, Joong Hee Lee^{a,c,**}

^a Department of Nano Convergence Engineering, Jeonbuk National University, Jeonju, Jeonbuk 54896, Republic of Korea

^b Division of Science Education, Graduate School of Department of Energy Storage/Conversion Engineering, Jeonbuk National University, Jeonju, Jeonbuk 54896 Republic of Korea

^c Carbon Composite Research Center, Department of Polymer-Nano Science and Technology, Jeonbuk National University, Jeonju, Jeonbuk 54896, Republic of Korea

ARTICLE INFO

Keywords:

Water splitting
Urea electrolysis
Adjutant Rh
Co₃S₄/CoO_x nanotubes
Multifunctional catalysts

ABSTRACT

In this work, smart strategies are conducted to design advanced multifunctional electrocatalysts: Co₃S₄/CoO_x heterostructured nanosheets-assembled nanotube arrays on 3D framework integrated with single Rh atoms and subnanometer clusters. The catalyst can reach current density of 10 mA cm⁻² at low overpotentials of 248.2, and 56.1 mV for oxygen evolution reaction, and hydrogen evolution reaction, respectively. The catalyst also shows very low potential of 1.32 V for urea oxidation reaction at 10 mA cm⁻². A water electrolyzer that achieves current density of 10 mA cm⁻² at small cell voltage of 1.45 V is prepared under action of the developed catalyst. We also conduct urea electrolysis assembled with the catalyst and find that the device requires a cell voltage of only 1.35 V to drive a current density of 10 mA cm⁻², proving the great potential of our catalyst for simultaneous energy-saving H₂ production and the treatment of urea-rich wastewater.

1. Introduction

Exploring and developing methods of high-purity hydrogen (H₂) production that meet the requirements of environment friendliness and economy is of great significance for the future H₂ economy [1]. The green method of H₂ production of electrochemical water electrolysis realized through cathodic hydrogen evolution reaction (HER) and anodic oxygen evolution reaction (OER) is highly interesting, as a consequence of its low energy consumption and green nature [2,3]. Another energy-saving strategy to produce H₂ is urea analysis assisted by the HER and anodic urea oxidation reaction (UOR), with the much smaller thermodynamic voltage of 0.37 V relative to that of OER in water electrolysis (1.23 V); the urea electrolysis is therefore both a more efficient method of H₂ production and an effective approach to treating urea-rich wastewater [4,5]. Even though precious metal-based electrocatalysts, such as Pt, Ru, and Ir, show remarkable electrocatalytic performances for water and urea splitting, their commercialization has always been bottlenecked by the serious limitations of these catalysts,

such as scarcity, high price, and insufficient stability [6–8]. Accordingly, pursuing multifunctional electrocatalysts with economical feature, high electrocatalytic performance, and good robustness for all HER, OER, and UOR towards promoting both water and urea electrolysis is vital to the perspective of green and energy-saving H₂ generation, as well as urea-containing wastewater treatment.

In recent years, transition metal sulfides (TMSs) have been explored and widely applied as cost-effective electrocatalysts for OER, UOR, and HER in water and urea splitting [9–11]. The morphological characteristics and electronic structure of electrocatalysts have been regarded as two essential parameters that affect electrocatalytic performance, thereby the smart strategies for improving the catalytic activity of TMSs towards outperforming the precious metal-catalysts should be pushed to the limit of these factors. On the one hand, many research attempts have been made to enhance the density of accessibly active centers, as well as the specific surface area of TMSs, by designing and constructing various morphological structures for extraordinary catalytic efficiency [12–14]. Amongst these structures, the 3D nanotube arrays (NTs) structure has

* Corresponding author.

** Corresponding author at: Department of Nano Convergence Engineering, Jeonbuk National University, Jeonju, Jeonbuk 54896, Republic of Korea.

E-mail addresses: nhk@jbnu.ac.kr (N.H. Kim), jhl@jbnu.ac.kr (J.H. Lee).

received considerable attention, and recently emerged as a good candidate for high-efficiency water and urea electrolysis, due to its synergy of two structural components. The 3D nanostructured architecture has very good capability for fast electrocatalytic reactions that originates from its open structure with abundance of hole spaces and effective channels, which thus supply a desirable specific surface area for electron transfer, as well as mass transport [15,16]. Meanwhile, nanosheets (NSs)-assembled NTs have recently received considerable attention from researchers, because of their high surface-volume ratio to enhance the penetration interface between catalyst and electrolyte, offering interconnected channels as low-resistance pathways to boost the electron transfer rate along the entire 1D nanotube, and reducing the utilization of precursor metals to reduce the cost [17,18]. In addition to the suitable morphology, improving the electronic conductivity of TMSs is also necessary for electrocatalytic performance. In this context, the integration of a conductive phase into TMSs offers an effective method. Transition metal oxides (TMOs) with their high capability for electron transfer have emerged as good candidates [19,20]. The theoretical and experimental works of X. Wang et al. have demonstrated that the interface between cobalt sulfide and cobalt oxide facilitated the increase in catalytic active sites and promoted the chemical adsorption/desorption of intermediate species during the process of electrocatalysis [21]. It is demonstrated that constructed heterostructure of TMSs and TMOs has great potential for electrochemical reactions, which is due to the excellent merits of this structure included exposure of more catalytically active sites, as well as accessible edges, excellent electrical conductivity, superior stability, having optimal electronic structure for facilitating charge transfer and adsorption/desorption of intermediates, and possessing synergistic effect. Thus, to minimize the overpotentials of the electrocatalytic reactions and raise the catalytic efficiency, in situ anchorage of TMSs/TMOs NTs on the 3D nanostructured framework is confidently anticipated to generate an advanced electrocatalytic material.

On the other hand, there has been an effort to use foreign metals as adjuncts to regulate the electronic structure of TMSs towards accelerating the reaction kinetics. X. Han et al. exhibited by both experimental and DFT calculations that in comparison with pure CoS_2 and Pt incorporation into CoS_2 surface, the synergy of Pt and CoS_2 could optimize hydrogen adsorption/desorption properties, facilitate the formation of OER active centers, and thus enhance the overall water splitting efficiency [22]. J. Wang et al. showed that the replacement of single atom Ru for Mo atoms led to exposure of more active sites and the formation of some vacancies, which thus improved the HER activity of MoS_2 ; DFT calculation also demonstrated the decrease in Gibbs free energy of H-adsorption after the incorporation of Ru into MoS_2 [23]. In another study, H. Xu et al. reported that the doping of Mo into Ni_3S_2 could redistribute the electronic and morphological structure, leading to the exposure of more active centers, as well as optimizing the Gibbs free energy of intermediates in the UOR, and thereby boosting the urea electrolysis performance [24]. Although promising results have been reported in recent years, reaching excellent catalytic behavior towards approaching the good activities of precious metal-based catalysts for TMSs is still a great challenge. The above considerations inspire us to develop advanced electrocatalysts for the HER, OER, and UOR through the integration of TMSs and an adjustable metal.

The sulfides and oxides of cobalt (Co_3S_4 and CoO_x) have recently been recognized as supplying appealing electrocatalysts for HER, OER, and UOR, as a result of their quintessential advantages [25,26]. Meanwhile, Rh can provide an excellent adjustable candidate for the host materials, which can be assigned to its high capability for water dissociation during the electrolysis process, and its strong affinity with adsorbed H atoms to boost the desorption of H_2 gas from catalyst surface [14,27]. Accordingly, in this study we report a trifle of adjustable Rh in the form of single atoms and subnanometer clusters dispersed on $\text{Co}_3\text{S}_4/\text{CoO}_x$ heterostructured NSs-assembled NTs to design heterostructured catalyst vertically grown on high-conductive 3D copper

framework (3D-CF) (denoted as $\text{Rh-Co}_3\text{S}_4/\text{CoO}_x$ NTs). Benefiting from remarkable physicochemical advantages, the developed catalyst displays extraordinary electrocatalytic efficiency and robust stability toward OER and HER in overall water splitting, as well as UOR and HER in full urea electrolysis, which are two key methods of green and energy-saving H_2 production.

2. Experimental section

2.1. Chemical reagents

Sodium hydroxide (NaOH , $\geq 97.0\%$), ammonium persulfate ($(\text{NH}_4)_2\text{S}_2\text{O}_8$, $\geq 98.0\%$), copper foam, acetone (CH_3COCH_3 , $\geq 99.5\%$), ethanol ($\text{C}_2\text{H}_5\text{OH}$, 25%), acetic acid (CH_3COOH , $\geq 99.0\%$), cobalt(II) chloride hexahydrate ($\text{CoCl}_2 \cdot 6\text{H}_2\text{O}$, 98.0%), sodium hydrosulfite ($\text{Na}_2\text{S}_2\text{O}_4$, $\geq 82.0\%$), sodium sulfide nonahydrate ($\text{Na}_2\text{S} \cdot 9\text{H}_2\text{O}$, $\geq 99.99\%$), ammonium hexachlororhodate (III) ($(\text{NH}_4)_3\text{RhCl}_6$), potassium hydroxide (KOH , $\geq 85.0\%$), urea (NH_2CONH_2 , $\geq 99.5\%$), commercial Pt/C (20 wt% of Pt), ruthenium (IV) oxide (RuO_2 , 99.9%), and Nafion solution (5 wt%) were purchased from Sigma Co. (USA).

2.2. Fabrication of $\text{Rh-Co}_3\text{S}_4/\text{CoO}_x$ NTs sample

Initially, the $\text{Cu}(\text{OH})_2$ nanoneedle arrays (denoted as $\text{Cu}(\text{OH})_2$ NNs) sample was synthesized according to our previously reported synthetic procedure [28]. The obtained $\text{Cu}(\text{OH})_2$ NNs was then transformed into CuO nanorods (denoted CuO NRs) by annealing under an air atmosphere at 350°C for 2 h. Next, the achieved CuO NRs was dipped into a reactant solution containing 0.6 g of $\text{CoCl}_2 \cdot 6\text{H}_2\text{O}$ and 100 mL of DI water. After mild stirring for 0.5 h, 94 mL of ethanol solution of $\text{Na}_2\text{S}_2\text{O}_4$ (ethanol/water = 4/5, v/v) was gradually dropped into the above reaction system under magnetic stirring condition, and after continuously stirring for 2 h, the colorless solution turned into ink purple color. Subsequently, the product was taken out of the reaction solution, cleaned by using DI water and ethanol for 3 times each, and dried at 60°C for 12 h prior to calcination at 400°C for 2 h under Ar flow; the CoO_x nanotubes (CoO_x NTs) was generated. Next, sulfidation process was conducted for the achieved CoO_x NTs by dipping in 0.01 M Na_2S solution at 90°C for 2 h to form $\text{Co}_3\text{S}_4/\text{CoO}_x$ NTs. After washing with DI water and ethanol for 3 times each and drying at 60°C overnight, such $\text{Co}_3\text{S}_4/\text{CoO}_x$ NTs was immersed in 0.04 mM $(\text{NH}_4)_3\text{RhCl}_6$ solution for 20s, followed by calcination under Ar atmosphere at 300°C for 2 h. Finally, the advanced $\text{Rh-Co}_3\text{S}_4/\text{CoO}_x$ NTs catalyst was formed. The comparative samples, including CuO NRs, CoO_x NTs, and $\text{Co}_3\text{S}_4/\text{CoO}_x$ NTs, were also individually prepared following the above protocol for further use in electrochemical measurements.

2.3. Material characterization

The field-emission scanning electron microscopy (FE-SEM) and energy dispersive X-ray analysis (EDAX) were realized on the Carl Zeiss-Gemini 500 instrument equipped with an EDX detector (Germany). Transmission electron microscopy (TEM) and high-resolution TEM (HR-TEM) were performed on JEOL-JEM 2010 instrument (Japan). The microstructure of samples was further investigated by high-angle annular dark-field scanning TEM (HAADF-STEM) analysis using Cs-corrected Field Emission TEM/STEM equipped with CCD camera and energy dispersive spectroscopy (EDS) detectors performed on JEOL-JEM ARM200F instrument (Japan). The crystallographic structures of the fabricated samples were determined using X-ray diffraction (XRD) analysis (PANalytical-X'Pert PRO Multi-Purpose X-Ray Diffractometer, Netherlands) at the Center for University-Wide Research Facilities (CURF), Jeonbuk National University (Korea). X-ray photoelectron spectroscopy (XPS) spectra were collected using Thermo Fisher Scientific-Theta Probe instrument (USA) in the Jeonju center of KBSI. To visualize the porosity and textural characteristics of samples, we also

conducted analysis of nitrogen adsorption-desorption isotherms using Micromeritics Instrument-ASAP 2020 Plus system (USA). In addition, we evaluated the wettability of the as-prepared materials by measuring the dynamic electrolyte contact angle using a Drop Shape Analyzer (DSA100E).

2.4. Electrochemical characterization

All electrochemical experiments were carried out on a CH660D workstation (CH Instruments Inc., USA) using a classic three-electrode electrochemical cell, in which a graphite rod, Ag/AgCl, and the as-synthesized samples (1 cm × 1 cm) were employed as the counter, reference, and working electrodes, respectively. 1.0 M KOH was used as electrolyte for OER, HER, and the overall water electrolysis, while 1.0 M KOH + 0.5 M urea was used as electrolyte for UOR and urea electrolysis. All potentials in this study are reported on the reversible hydrogen electrode (RHE) scale. The calibration of Ag/AgCl electrode to RHE was

performed according to the following equation [29]:

$$E_{RHE} = E_{Ag/AgCl} + 0.059pH + E_{Ag/AgCl}^0 \quad (1)$$

where $E_{Ag/AgCl}^0 = 0.1976$ V (at 25 °C).

The linear sweep voltammetry (LSV) curves were recorded at a scan rate of 5 mV s⁻¹. Note that all potentials of the LSV curves for HER, OER, and UOR were compensated for Ohmic drops using the previously reported equation [6]:

$$E_{iR-corrected} = E_{measured} - I \times R_s \quad (2)$$

where, R_s is the series resistance measured from the electrochemical impedance spectroscopy (EIS) analysis. Multi-step chronopotentiometric measurements were carried out in overpotential ranges of (248.2–331.1) mV vs. RHE for OER, (56.5–169.8) mV vs. RHE for HER, and potential range of (1.32–1.45) V vs. RHE for UOR. Long-term stability tests were performed at standard overpotentials of 124.2 mV vs. RHE for the HER, 300.5 mV vs. RHE for the OER, potentials of 1.41 V vs.

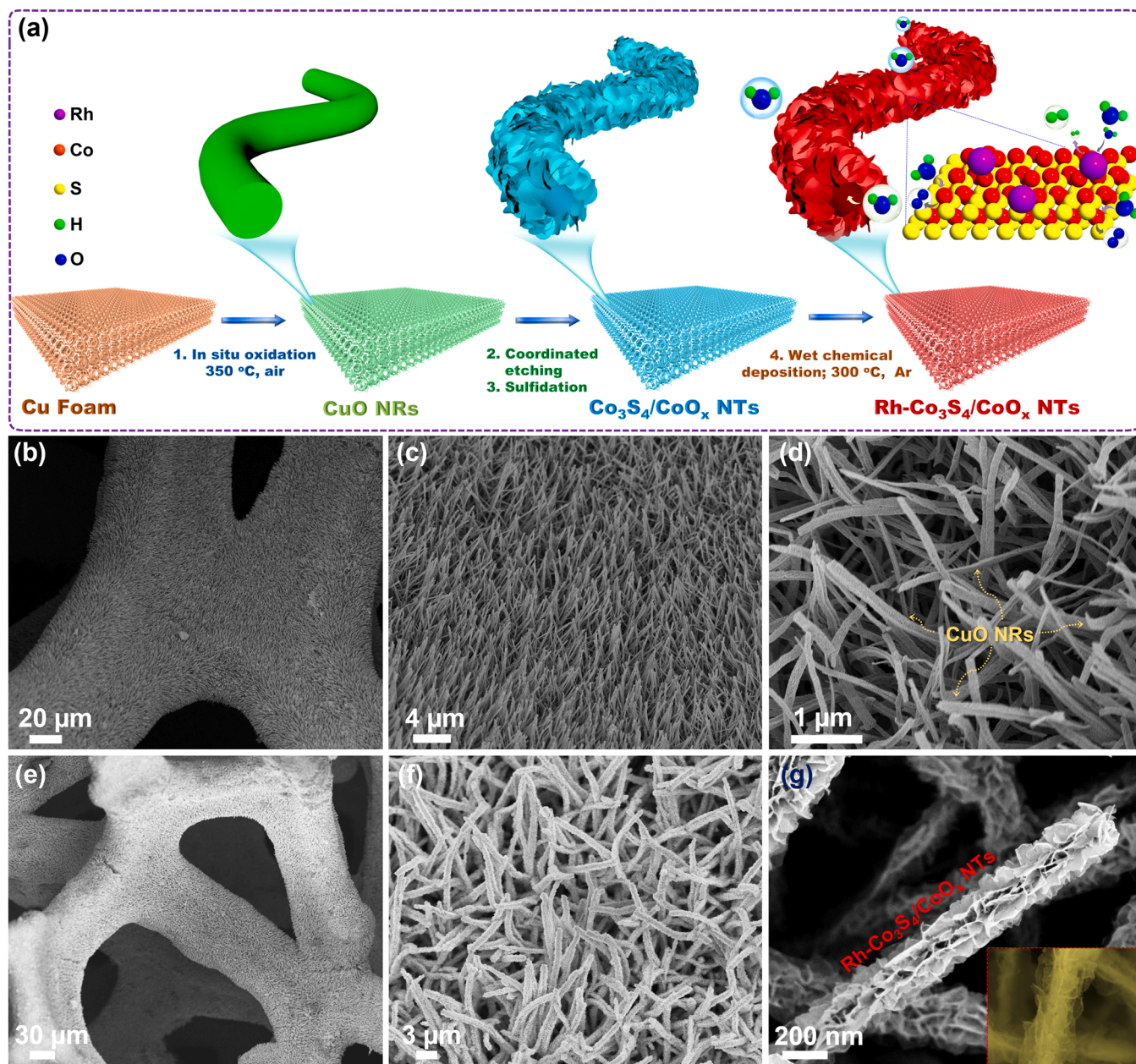


Fig. 1. (a) Schematic illustration showing the synthesis procedure of Rh-Co₃S₄/CoO_x NTs. FE-SEM images of (b-d) the CuO NRs and (e-g) Rh-Co₃S₄/CoO_x NTs.

RHE for the UOR, 1.55 V vs. RHE for the overall water electrolysis, and 1.48 V vs. RHE for the urea electrolysis. Electronic double layer capacitance (C_{dl}) was obtained from the cyclic voltammetry (CV) measurement; in this work, the CV curves were recorded over a non-Faradic potential range for all the OER, UER, and HER at unequal scan rates of 10, 15, 20, 25, and 30 mV s⁻¹. The EIS was realized from 10⁵ to 10⁻² Hz at an overpotential originated from the current density of 10 mA cm⁻² for all HER, OER, and UOR. The Faradaic efficiency (FE) was confirmed by the following equation [30]:

$$FE = \frac{V_m}{V_t} \quad (3)$$

where, V_m is the volume of the produced gas (L), and V_t is the molar volume (L, 24.5 L mol⁻¹, RT).

3. Results and discussion

3.1. Morphological and structural characterization

The Rh-Co₃S₄/CoO_x NTs sample was simply prepared by a template-assisted approach combined with wet chemical method, as provided in Fig. 1a. Initially, Cu(OH)₂ nanoneedles were successfully deposited on the surface of 3D-CF framework via the in situ oxidation of copper in alkaline environment, which was identified by FE-SEM analysis. Fig. S1 shows that the highly conductive 3D-CF cage has a rather smooth surface with abundant open holes at the micrometer scale, on which the well-aligned Cu(OH)₂ nanoneedles are densely dispersed. Such Cu(OH)₂ nanoneedles possess a relatively smooth surface with diameters of about 100–200 nm. Following that, the Cu(OH)₂ nanoneedles was converted into CuO nanorod by a thermal calcination route. The SEM images in Fig. 1b–d indicate that most of the morphological features of the original Cu(OH)₂ nanoneedles are retained after annealing, but the surface roughness of nanorod is enhanced, which can be attributed to the water removal during the calcination stage at 350 °C. In the next step, the CuO NRs template was etched, and at the same time, Co(OH)₂ NSs was vertically regrown along the entire length of the CuO NRs core to form the Co(OH)₂ NSs-assembled NTs via a coordinated etching and precipitation approach [31]. After calcinating to form CoO_x NTs, the SEM images in Fig. S2 show that the structural array of the original CuO NRs templates was well replicated in the CoO_x NTs sample, on which the diameters of CoO_x NTs are found to be around 200–220 nm, slightly larger than that of the CuO NRs. It is obvious that these CoO_x NTs are assembled from many CoO_x NSs, as shown in the highly-magnified SEM imagery (Figs. S2c and d); also, there is no solid nanorod morphology in the as-synthesized CoO_x NTs sample, suggesting the complete decomposition of the original CuO NRs templates, as well as the successful formation of CoO_x NTs of tubular nature during this conversion step.

A subsequent sulfidation reaction was then performed to transform the CoO_x NTs into Co₃S₄/CoO_x NTs (Fig. S3), which reveals a similar morphology to that of the 3D NSs-assembled NTs of the precursor CoO_x NTs. Finally, wet chemical deposition combined with annealing was conducted to deposit single Rh atoms and subnanometer clusters over the surface of the Co₃S₄/CoO_x NTs, leading to the formation of the last Rh-Co₃S₄/CoO_x NTs heterostructure sample. The SEM imagery of Rh-Co₃S₄/CoO_x NTs at different magnifications (Fig. 1e–g) exhibit that this sample possesses all the morphological characteristics of the original Co₃S₄/CoO_x NTs, including the nanotube array structure and tubular feature. This observation proves that the quintessential morphological structure of the original Co₃S₄/CoO_x NTs remains remarkably unaffected by the step of Rh growth. The structural characteristics of nanotube arrays with high surface-volume ratio help enlarge the catalyst-electrolyte interface for electrocatalytic reactions, electrolyte penetration, and the release of gaseous species produced during the catalytic process. Meanwhile, the morphological characteristics of the 3D NTs can supply conducting pathways for efficient charge transfer, the expected

specific surface area with abundant accessible reaction centers, and open space for facilitating mass transport towards the remarkably enhanced efficiency of the catalytic water and urea electrolysis. The chemical composition changes in the samples at each fabrication stage were then investigated by EDAX, as shown in Fig. S4, which again confirms the successful formation of the above-mentioned samples.

The micro-morphological characteristics of the as-synthesized Rh-Co₃S₄/CoO_x NTs sample were investigated by TEM measurement. Fig. 2a exhibits a typical TEM image of the individual Rh-Co₃S₄/CoO_x nanotube, displaying the well-preserved one-dimensional (1D) structure and homogeneous Rh-Co₃S₄/CoO_x NSs assembling vertically along the entire etched 1D template to form the morphological feature of nanotube. The diameter of the Rh-Co₃S₄/CoO_x nanotube is found to be ~ 250 nm, which is confirmed by the SEM. Further, the thin property of the Rh-Co₃S₄/CoO_x NSs is identified by their transparent characteristic, as shown in the magnified TEM image (Fig. 2b); such low thickness property of nanosheet may induce the entire material to offer very low contact resistance and enhanced accessible surface area, expecting to significantly improve the electrocatalytic performance of the material for all OER, UOR, and HER processes. HR-TEM is carried out to further disclose the structural property of the Rh-Co₃S₄/CoO_x NTs material on the atomic scale. The HR-TEM image taken at the outer Rh-Co₃S₄/CoO_x layer (Fig. 2c) displays two well-resolved lattice fringes with interplanar distances of ~ 0.20 and ~ 0.246 nm associated with the (111) and (111) planes of Co and CoO, respectively [32,33], suggesting the presence of CoO_x phase (x = 0 and 1) in this structure. Meanwhile, the other lattice fringes with inter-planar distance of about ~ 0.329 nm could be well attributed to the (220) plane of Co₃S₄ [34]. Notably, there is one obvious crystal boundary highlighted by the red line between the CoO and the Co₃S₄, confirming the representative existence of a nano-scale heterostructure. Such interface between cobalt sulfide/oxide has been demonstrated to be beneficial to the adsorption and desorption of hydrogen/oxygen intermediates of the electrochemical reactions, and thus favor the process of electrolysis [19]. The HR-TEM shows only lattice fringes belonging to the Co, CoO, and Co₃S₄ phases, proving the representative formation of single Rh atoms and subnanometer clusters in this structure, which is confirmed by the corresponding HAADF-STEM imagery as well (Fig. 2d–f). Indeed, a dense dispersion of bright spots over the surface of the Co₃S₄/CoO_x nanosheet are visually observed in the HAADF-STEM image (Fig. 2d); these bright spots can be attributed to the Rh atoms, due to the difference of Z-contrast between the heavier Rh atoms and lighter Co atoms [35]. The detail of the form of the Rh was further studied by HAADF-STEM measurements at high magnifications (Fig. 2e and f). Many visible single atomic Rh species marked with yellow arrows, together with several Rh subnanometer clusters marked with yellow circles with mean sizes in the range (0.5–0.7) nm, can be clearly observed, and are highly distributed on the surface of Co₃S₄/CoO_x NSs substrate. These results confirm the coexistence of single Rh atoms and sub-nano clusters in the proposed sample, which may result in enhancing the utilization efficiency of Rh, along with reducing the amount of metal precursor used towards lowering the cost of the obtained material. Such atomic dispersion of Rh is also expected to generate more catalytic active sites for electrocatalytic reactions, in comparison to the other larger forms. Scanning TEM (STEM) and EDS elemental mapping imagery proves the existence of the four required elements of Co, S, O, and Rh (Fig. 2g–i), which are homogeneously dispersed over the entire as-synthesized nanotube, corroborating the successful fabrication of the Rh-Co₃S₄/CoO_x NTs material via our effective approach.

The XRD analysis was conducted to acquire more detailed crystalline phase information of the produced materials. The XRD pattern of Cu(OH)₂ NNs (Fig. S5) well confirms that all diffraction peaks are indexed to Cu(OH)₂ phase (PDF#80–0656), except for the typical peaks of 3D-CF substrate (PDF#04–0836) [36,37]. The appearance of CuO diffraction peaks (PDF#45–0937), instead of the characteristic peaks of Cu(OH)₂ in the CuO NRs sample (Fig. S5) proves the successful transformation of Cu

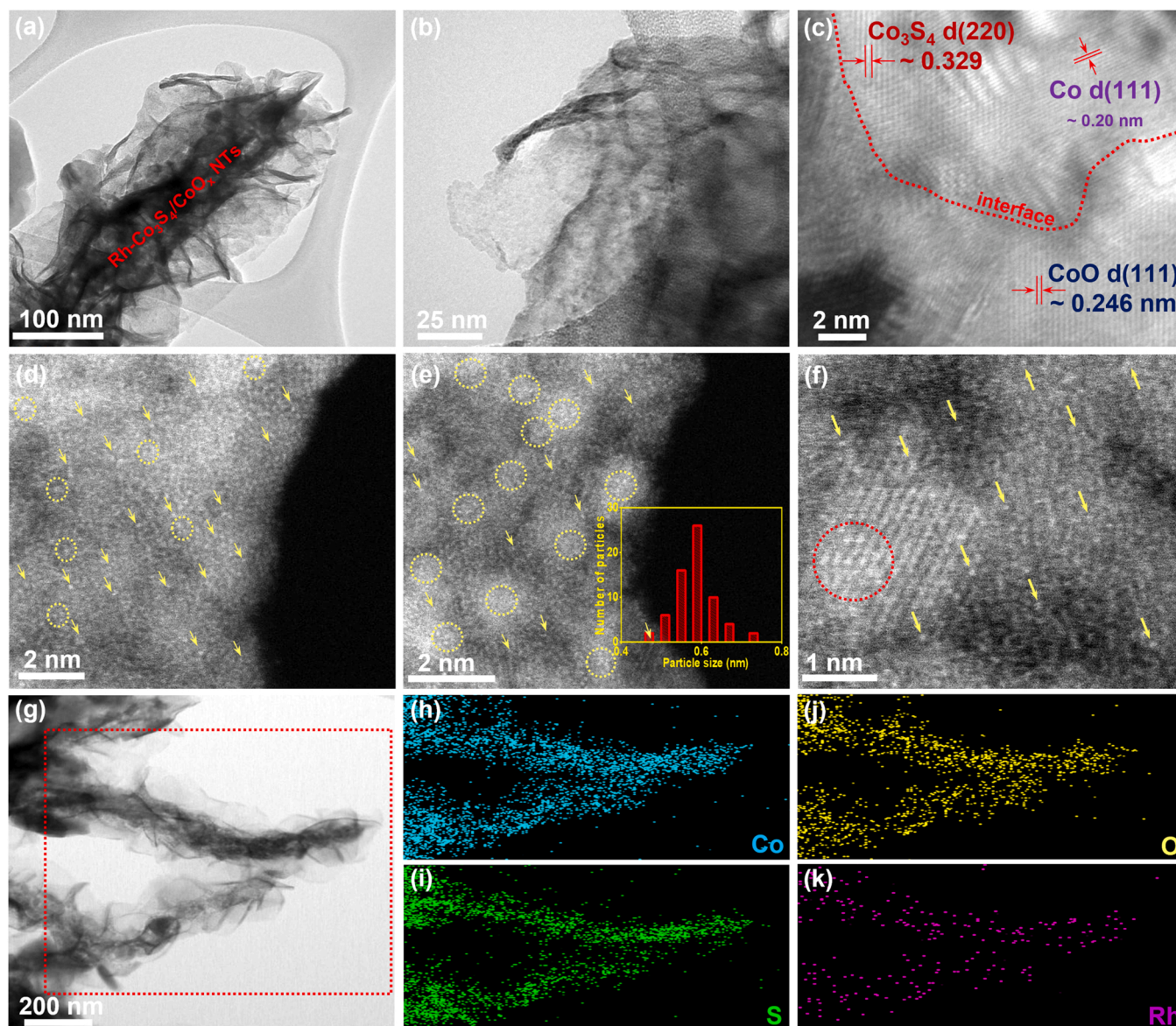


Fig. 2. (a and b) TEM and (c) HR-TEM images of the Rh- $\text{Co}_3\text{S}_4/\text{CoO}_x$ NTs. (d-f) HAADF-STEM images taken at Rh- $\text{Co}_3\text{S}_4/\text{CoO}_x$ layer at different magnifications. (g) STEM image of the Rh- $\text{Co}_3\text{S}_4/\text{CoO}_x$ NTs. EDS elemental mapping images of the Rh- $\text{Co}_3\text{S}_4/\text{CoO}_x$ NTs for (h) Co, (i) S, (j) O, and (k) Rh.

(OH)₂ into CuO via the annealing step at low temperature in air atmosphere [38]. Meanwhile, apart from the 3D-CF diffractions, the XRD pattern of CoO_x NTs (Fig. S5) exhibits only the diffraction peaks belonging to Co (PDF#15–0806) and CoO (PDF#75–0418), indicating that the template CuO NRs are fully etched to generate hollow interior, while the outer CoO_x NSs ($x = 0$ and 1) are successfully grown over such template surfaces as well [39,40]. The diffraction peaks in the XRD patterns of $\text{Co}_3\text{S}_4/\text{CoO}_x$ NTs and Rh- $\text{Co}_3\text{S}_4/\text{CoO}_x$ NTs (Fig. 3a) well demonstrate that the peaks of these materials should be attributed to Co_3S_4 (PDF#47–1738), Co, and CoO phases [41]. Apart from these, no other typical peaks for Rh-based compounds, such as rhodium sulfides, alloys of Rh, rhodium oxides/hydroxides, or metallic Rh, can be identified in the XRD pattern of the Rh- $\text{Co}_3\text{S}_4/\text{CoO}_x$ NTs material, favorably evidencing the generation of single Rh atoms and subnanometer clusters within this structure, which should be attributed to the very low content of Rh element.

Further examination of the chemical composition and electronic interactions was performed by XPS analysis. Fig. 3b compares the survey XPS spectra of Rh- $\text{Co}_3\text{S}_4/\text{CoO}_x$ NTs and $\text{Co}_3\text{S}_4/\text{CoO}_x$ NTs, and shows that they both contain Co 2p, O 1s, and S 2p orbitals that originate from Co,

CoO, and Co_3S_4 phases. Additionally, the appearance of Rh 3d orbital in only the Rh- $\text{Co}_3\text{S}_4/\text{CoO}_x$ NTs reconfirms the successful deposition of single Rh atoms and sub/nanoclusters in this structure. Fig. 3c-g present the high-resolution XPS spectra of Rh 3d, Co 2p, S 2p, and O 1s regions for the Rh- $\text{Co}_3\text{S}_4/\text{CoO}_x$ NTs. Regarding the Rh 3d region, two peaks that emerge at binding energies of 309.3 and 314.1 eV are assigned to the oxidized Rh species derived from the bonding between the Rh cluster surfaces and oxygen species, which cannot be prevented in the air [27]. As for the high-resolution XPS spectrum of Co 2p, the Co 2p can be deconvoluted into two primary regions that include the Co 2p_{3/2} region with the peaks located at the binding energies of 778.22, 779.09, 781.41, and 786.17 eV, and the Co 2p_{1/2} region with the peaks appearing at 794.04, 794.78, 796.87, and 803.20 eV. In the detail of Co 2p, a pair of peaks at 778.22 and 794.04 eV can be attributed to the Co⁰ of metallic Co [42], while two pair of peaks located at (779.09 and 794.78) and (781.41 and 796.87) eV, respectively, correspond to the Co³⁺ and Co²⁺ of the Co_3S_4 and CoO phases [43–45]. The emergence of two characteristic satellite peaks (denoted as sat.) at 786.17 and 803.2 eV strongly supports the formation of Co²⁺ oxidation state within the Rh- $\text{Co}_3\text{S}_4/\text{CoO}_x$ NTs structure, reconfirming the presence of Co_3S_4

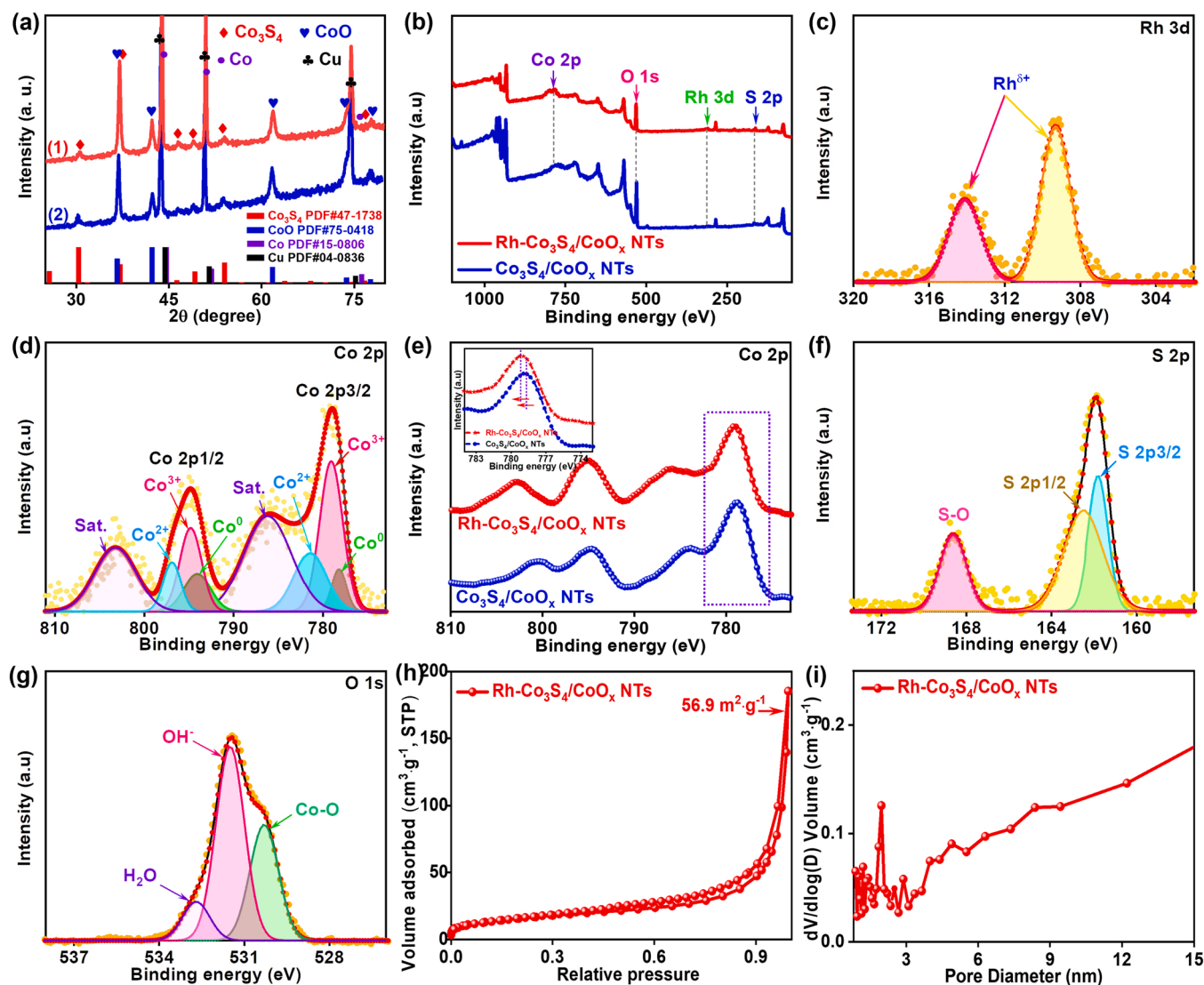


Fig. 3. (a) XRD patterns (1): Rh-Co₃S₄/CoO_x NTs and (2) Co₃S₄/CoO_x NTs and (b) XPS survey spectra of the Rh-Co₃S₄/CoO_x NTs and Co₃S₄/CoO_x NTs. (c) High-resolution XPS spectrum of Rh 3d for the Rh-Co₃S₄/CoO_x NTs. (d) High-resolution XPS spectrum of Co 2p for the Rh-Co₃S₄/CoO_x NTs. (e) Comparison of Co 2p binding energy between the Rh-Co₃S₄/CoO_x NTs and Co₃S₄/CoO_x NTs; inset of figure e: comparison of Co 2p_{3/2} binding energy between the Rh-Co₃S₄/CoO_x NTs and Co₃S₄/CoO_x NTs. (f) High-resolution XPS spectrum of S 2p for the Rh-Co₃S₄/CoO_x NTs. (g) High-resolution XPS spectra of O 1s for the Rh-Co₃S₄/CoO_x NTs. (h) N₂ adsorption-desorption curve and (i) porous size distribution of the Rh-Co₃S₄/CoO_x NTs.

and CoO [46]. For the purpose of comparison, Fig. 3e provides the XPS spectra of the Co 2p regions for both Rh-Co₃S₄/CoO_x NTs and Co₃S₄/CoO_x NTs. A positive shift of around 0.48 eV of Co 2p_{3/2} in the Rh-Co₃S₄/CoO_x NTs is evident, compared to that observed in the Co₃S₄/CoO_x NTs, suggesting a redistribution of electron density around Co atoms after the introduction of adjutant Ru species, due to the pulling of partial electron from lower-electronegativity Co atoms to higher-electronegativity Rh. As a result, the electron density around Co becomes lower, leading to the increased electron affinity of Co, and thus benefiting the adsorption of negative intermediates: OH⁻ of the OER process and (NH₄)₂CO⁻ of the UOR process, towards boosting the OER and UOR performance [47,48]. In contrast, the extraction of electron from neighboring Co atoms enriches the electron density around Rh, bringing Rh species an optimal capability in the adsorption of positive intermediate: H⁺ of the HER reaction, together with the enhancement of charge transfer for the HER, and at the same time, improving HER performance [48]. Therefore, the introduction of adjutant Rh brings the variation of electronic structure of both the guest Rh and host Co atoms; these variations have been well known as advantageous factors for water

and urea electrolysis. Otherwise, the formation of Co₃S₄ phase is once again confirmed through the XPS spectra of the S 2p region. Two dominate peaks emerging at 161.8 and 162.5 eV agree well with S 2p_{3/2} and S 2p_{1/2}, respectively, of the Co₃S₄; the additional peak at 168.66 eV can be assigned to the S-O binding, which is because of the partial oxidation of Co₃S₄ in air [49]. The O 1s XPS spectrum in Fig. 3g reveals the peaks at 530.3 eV, identifying the existence of Co-O bonding. Meanwhile, two peaks at 531.5 and 532.7 eV correspond to the adsorbed OH⁻ and adsorbed water on the surface of the catalyst, respectively [8].

The specific surface area and textural property of the Rh-Co₃S₄/CoO_x NTs sample was tested by N₂ adsorption/desorption measurement. Fig. 3h shows that all characteristics of the obtained curve belong to a typical type IV isotherm; further, a visible hysteresis loop ranging 0.3–1.0 relative pressure within the thermal curve demonstrates the presence of excellent mesoporous structure in the developed sample. The Rh-Co₃S₄/CoO_x NTs can reach to a large specific surface area of 56.9 m² g⁻¹, which is much larger than those of the literature (Co₃S₄@FNC-Co4 with 30 m² g⁻¹ [50], Co₃S₄ with 46.2 m² g⁻¹ [51], Co₃S₄

@Co₃O₄ core-shell with 13.0 m² g⁻¹ [49], CuCo₂S₄ nanosheet with 37.6 m² g⁻¹ [52], etc.). Moreover, the pore size distribution illustrated in Fig. 3i exhibits that the pore diameter of Rh-Co₃S₄/CoO_x NTs is primarily concentrated in the range 1.65–2.35 nm, clearly in the mesoporous range (between 2 and 50 nm), which is further supportive evidence for its outstanding mesoporous feature. The exceptionally large surface area of the Rh-Co₃S₄/CoO_x NTs with excellent mesoporous structure enables the exposure of more accessible catalytic active sites on its surfaces and is favorable to the permeation of electrolyte/reactant into the inner catalytic centers, to finally improve the electrocatalysis efficiency.

3.2. Electrocatalytic performance

The as-synthesized Rh-Co₃S₄/CoO_x NTs was applied in OER conditions using a typical three-electrode configuration to assess its catalytic performance. The comparative tests were carried out with Co₃S₄/CoO_x

NTs, CoO_x NTs, CuO NRs, and commercial Pt/C catalyst. Fig. 4a–c represent LSV curves; corresponding Tafel plots; and comparison of the overpotentials at 10 mA cm⁻² current density and Tafel slopes between the Rh-Co₃S₄/CoO_x NTs and the comparative samples, respectively. To achieve the same current density of 10 mA cm⁻², the Rh-Co₃S₄/CoO_x NTs requires overpotential of 248.2 mV, which is 18.5, 41.1, and 104.2 mV lower those of the Co₃S₄/CoO_x NTs, CoO_x NTs, and CuO NRs, respectively. Furthermore, only 68.7 mV dec⁻¹ of Tafel slope can be found for the Rh-Co₃S₄/CoO_x NTs, while the Co₃S₄/CoO_x NTs, CoO_x NTs, and CuO NRs present much higher Tafel slope values of 96.0, 97.4, and 154.8 mV dec⁻¹, respectively. The increases in overpotentials and Tafel slope values following the trend of Rh-Co₃S₄/CoO_x NTs < Co₃S₄/CoO_x NTs < CoO_x NTs < CuO NRs demonstrate that the OER catalytic performance and reaction kinetics of the main Rh-Co₃S₄/CoO_x NTs sample are much better than those of the others, which should be assigned to the synergy of the 3D NTs feature with tubular structure, heterostructure of Co₃S₄/CoO_x with the formation of an effective metal

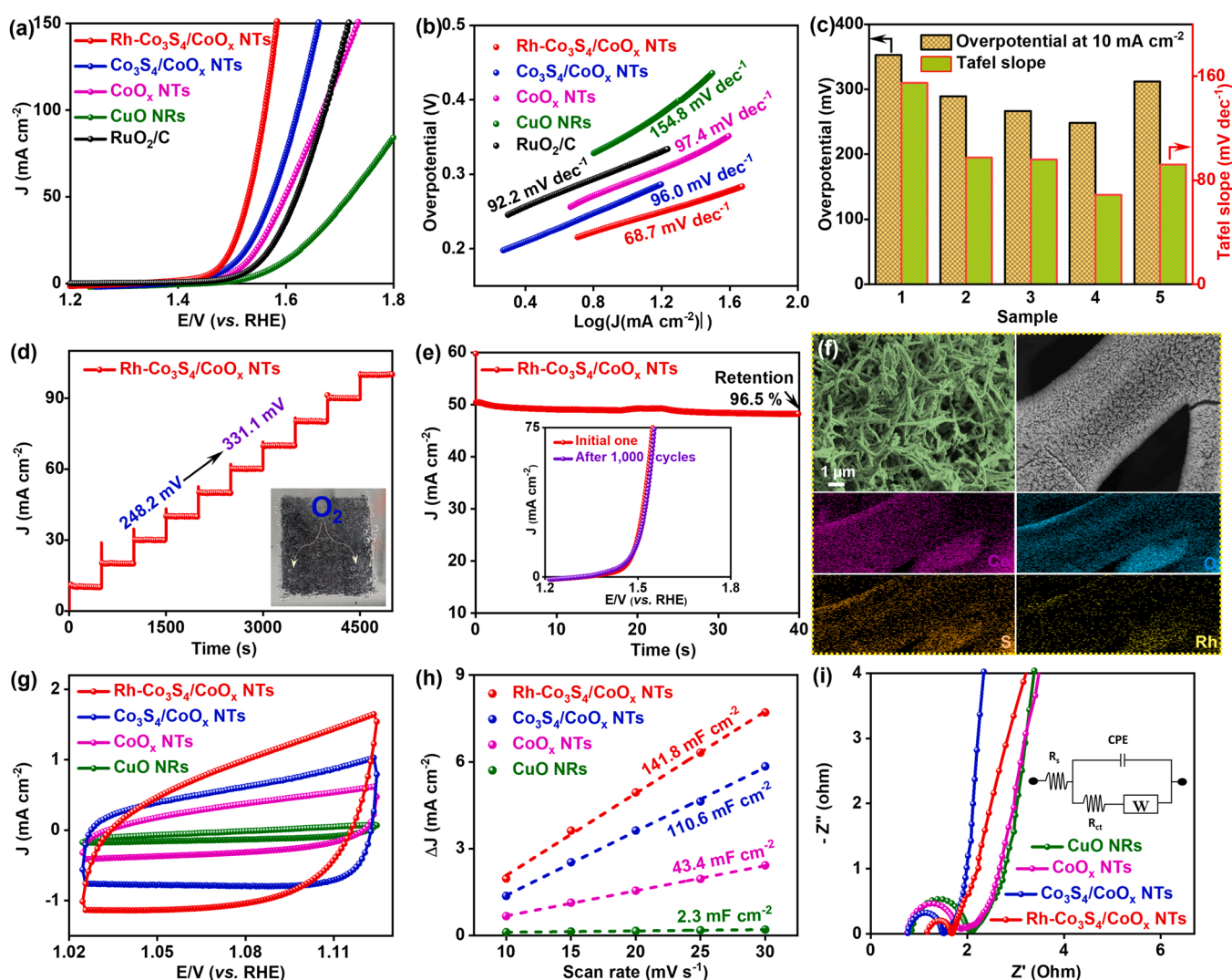


Fig. 4. Electrocatalytic activity of the as-prepared materials for the OER in alkaline conditions (1.0 M KOH): (a) *iR*-corrected LSV curves and (b) the corresponding Tafel plots of CuO NRs, CoO_x NTs, Co₃S₄/CoO_x NTs, Rh-Co₃S₄/CoO_x NTs, and RuO₂/C. (c) Comparison of overpotential and Tafel slope between the Rh-Co₃S₄/CoO_x NTs and the referenced materials ((1): CuO NRs, (2): CoO_x NTs, (3): Co₃S₄/CoO_x NTs, (4): Rh-Co₃S₄/CoO_x NTs, and (5): RuO₂/C). (d) Multi-step chronoamperometric curve of the Rh-Co₃S₄/CoO_x NTs; inset of figure d: photograph of Rh-Co₃S₄/CoO_x NTs electrode during the multi-step chronoamperometric testing. (e) Chronoamperometric curve of the Rh-Co₃S₄/CoO_x NTs; inset of figure e: LSV curves of the Rh-Co₃S₄/CoO_x NTs recorded before and after 1000 CV cycles. (f) SEM and EDS elemental mapping images of the post-OER Rh-Co₃S₄/CoO_x NTs. (g) CV curves of Rh-Co₃S₄/CoO_x NTs, Co₃S₄/CoO_x NTs, CoO_x NTs, and CuO NRs at a scan rate of 10 mV s⁻¹. (h) The current density variation ($\Delta J = J_{\text{anode}} - J_{\text{cathode}}$) at 1.0736 V vs. RHE) as a function of scan rates of the Rh-Co₃S₄/CoO_x NTs, Co₃S₄/CoO_x NTs, CoO_x NTs, and CuO NRs. (i) Nyquist plots of the Rh-Co₃S₄/CoO_x NTs, Co₃S₄/CoO_x NTs, CoO_x NTs, and CuO NRs; inset of i: an equivalent circuit to fit the Nyquist plots for evaluate R_{ct} and solution resistance.

sulfide/oxide interface, and the atomic effect of the Rh single atom/cluster within the Rh-Co₃S₄/CoO_x NTs. Currently, RuO₂ has been recognized as a benchmark electrocatalyst for the OER, with good catalytic and robust behavior. Regarding RuO₂ catalyst, the overpotential at current density of 10 mA cm⁻² is found to be 311.8 mV, and the Tafel slope is 92.2 mV dec⁻¹ in this work, which values are in good agreement with the literature [53,54]. Therefore, the proposed Rh-Co₃S₄/CoO_x NTs shows higher catalytic activity relative to the commercial RuO₂, which is considered an important factor in practical application at industrial scale, by lowering the cost and reducing environmental pollution. Further, the electrocatalytic performance of the Rh-Co₃S₄/CoO_x NTs for the OER is among the highest of the other OER catalysts reported elsewhere in term of overpotential and Tafel slope, as listed in Table S1. In addition to extraordinary catalytic behavior, stability is another essential parameter to evaluate whether the electrocatalysts possess potential for commercialization prospects. The stability of Rh-Co₃S₄/CoO_x NTs towards the OER was thus probed by conducting multipotential step measurements, as shown in Fig. 4d. It is worth noting that the current densities of Rh-Co₃S₄/CoO_x NTs remain constant without remarkable degradation for the rest of 500 s under each applied overpotential, suggesting excellent stability, superior mass transport, and mechanical strength of the Rh-Co₃S₄/CoO_x NTs catalyst in the process of OER [55]. The remarkable catalytic behavior of Rh-Co₃S₄/CoO_x NTs towards the OER is further supported by the formation of abundant oxygen (O₂) bubbles on its surface during the OER multipotential step test, as seen in the inset of Fig. 4d. The operation at a constant potential corresponding to 50 mA cm⁻² current density was also further prolonged to 40 h to assess the lifetime of the proposed Rh-Co₃S₄/CoO_x NTs catalyst under OER condition. The result in Fig. 4e displays that after the 40 h stability test, 96.5% of the initial current density is preserved, along with the good retention of catalytic activity proved by the almost overlapping LSV curves before and after 1000 CV cycles (inset of Fig. 4e). According to the SEM imagery of the post-OER Rh-Co₃S₄/CoO_x NTs (Fig. 4f), the virgin structural morphology of the catalyst is well retained in the long-term stability measurement. The EDS mapping images in Fig. 4f further confirm the excellent stability of Rh-Co₃S₄/CoO_x NTs by exhibiting that all the required elements in the initial catalysts structure, including Co, S, O, and Rh, are preserved. The XRD and XPS measurements were also performed for the post-OER Rh-Co₃S₄/CoO_x NTs, to investigate its structure in detail. The XRD patterns in Fig. S6a show that apart from the mainly CoO_x (Co and CoO) and Co₃S₄ phases, the post-OER material exhibits new phase CoOOH, which is attributed to the partial transformation of Co and Co₃S₄ to CoOOH during prolonged catalysis [45,50], which have been recognized as the additive catalytic active centers for the OER. The high-resolution XPS spectrum of Co 2p for the post-OER Rh-Co₃S₄/CoO_x NTs (Fig. S6c) indicates the slightly positive shifts of all the peaks in comparison to the initial one; further, the intensities of the metallic Co⁰, as well as Co²⁺ and Co³⁺, belonging to Co₃S₄ are significantly reduced after long-term operation, together with the formation of two new peaks centered at 781.3 and 795.8 eV for CoOOH, respectively [45]. The S 2p spectrum (Fig. S6d) also exhibits a decrease in densities of the peaks, which is likely due to a partial leaching of S element, which is associated with the in situ electrochemical oxidation of Co₃S₄ to form Co (oxy) hydroxide, as mentioned above. In contrast, the Rh 3d seems to be stable during the long-term OER process, and shows no clear change in the peak position, as well as intensity (Fig. S6f). Next, to further clarify the reason for the improved OER electrocatalytic performance of Rh-Co₃S₄/CoO_x NTs, the electrochemical surface area (ECSA) of the developed samples was assessed by testing their C_{dl} in the non-Faradaic zone. The CV curves in Fig. 4g and S7 display that the currents of the main Rh-Co₃S₄/CoO_x NTs sample are higher than those of its counterparts at the same scan rates, suggesting its highest C_{dl} values among the others. We found out that the C_{dl} of Rh-Co₃S₄/CoO_x NTs is 141.8 mF cm⁻², which is 31.2, 98.4, and 139.5 mF cm⁻² higher than those of the Co₃S₄/CoO_x NTs, CoO_x NTs, and CuO NRs, respectively (Fig. 4h). This result proves that the Rh-Co₃S₄/CoO_x

NTs can reach a much larger ECSA with more exposed accessible catalytic active species when compared to its counterparts, which should be recognized as the primary reason why the Rh-Co₃S₄/CoO_x NTs demonstrates better catalytic behavior for the OER. Apart from the enhancement of active site density, the proposed Rh-Co₃S₄/CoO_x NTs catalyst can offer a more favorable and faster charge transfer relative to its comparative samples during the process of OER, which is supported by EIS testing, as shown in Fig. 4i. As expected, the charge transfer resistance (R_{ct}) of the Rh-Co₃S₄/CoO_x NTs is calculated to be around 0.51 Ω through fitting its Nyquist plot in a proper circuit (inset of Fig. 4i), which is much lower than those of the Co₃S₄/CoO_x NTs, CoO_x NTs, and CuO NRs of 0.71, 1.13, and 1.22 Ω, respectively, confirming the improved reaction kinetics of OER that originate from the development of unique heterostructure with optimal electronic configuration.

Although the OER is an environment friendly process, its high thermodynamic oxidation potential of 1.23 V leads to significant increase in the energy consumption of overall water splitting, and thus replacement of the OER with the UOR, as an energy-saving reaction with a much lower thermodynamic potential of 0.37 eV is necessary to realize cost-effective hybrid water/urea electrolysis. In this context, we further assessed the catalytic activity of the Rh-Co₃S₄/CoO_x NTs for UOR in alkaline conditions (1.0 M KOH + 0.5 M urea), along with Co₃S₄/CoO_x NTs, CoO_x NTs, CuO NRs, and the benchmark RuO₂ catalyst, for comparison. As depicted in Fig. 5a, under UOR conditions, the Rh-Co₃S₄/CoO_x NTs requires much lower potentials than that under the traditional OER condition to achieve the same currents. Clearly, the Rh-Co₃S₄/CoO_x NTs can deliver current densities of 10 and 50 mA cm⁻² at the relatively low potentials of 1.32 and 1.40 V for the UOR, respectively, which are much smaller than those for OER (inset of Fig. 5a), suggesting that our well-constructed material can serve as a promising catalyst for the alternative anodic UOR process towards reducing the energy cost of H₂ production. More importantly, the UOR performance of the Rh-Co₃S₄/CoO_x NTs outperforms most electrocatalyst reported for the UOR, as listed in Table S2. When compared with the counterparts (Fig. 5b and S8), the UOR exhibits much lower potentials under the catalysis of Rh-Co₃S₄/CoO_x NTs, than those under the Co₃S₄/CoO_x NTs, CoO_x NTs, and CuO NRs of 1.37, 1.40, and 1.48 V, respectively, to gain the same current densities of 10 mA cm⁻². Furthermore, the Rh-Co₃S₄/CoO_x NTs also shows superior UOR catalytic activity to the benchmark RuO₂, which needs 1.39 and 1.46 V, as high as the potentials of our catalyst at current densities of 10 and 50 mA cm⁻², respectively. In addition, Tafel plot was used to clarify the UOR reaction kinetics of the Rh-Co₃S₄/CoO_x NTs and its counterpart electrodes. The results in Fig. 5c and S8 reveal that the Rh-Co₃S₄/CoO_x NTs proves a very small UOR Tafel slope of 51.6 mV dec⁻¹, which is considerably lower than that required for the traditional OER process (Table S2), and also surpasses the Tafel slopes of 91.3, 150.8, and 313.4 mV dec⁻¹ for the Co₃S₄/CoO_x NTs, CoO_x NTs, and CuO NRs, respectively. Such a smaller Tafel slope demonstrates the faster and more favorable catalytic kinetics of the UOR relative to the OER and confirms the improved UOR reaction kinetics under the catalysis of well-designed Rh-Co₃S₄/CoO_x NTs. The durability and stability of Rh-Co₃S₄/CoO_x NTs under the UOR condition was firstly investigated by using multi-step chronoamperometric measurement to observe the current density response under varying applied potential of 1.32–1.45 V vs. RHE. The multi-step chronoamperometric curve (Fig. 5c) displays that as the applied potential increases, the responding current density immediately changes to a stable value, and maintains unchanged for 500 s. This phenomenon occurs throughout the process testing event at the high supplied potentials, suggesting the excellent behavior of the Rh-Co₃S₄/CoO_x NTs in mass transport, such as electrolyte diffusion and the release of generated gaseous species, as well as its good conductivity and stability upon being catalyzed for the UOR reaction [4]. From the optical image of Rh-Co₃S₄/CoO_x NTs working electrode (inset of Fig. 5d), it is obvious that a very high density of gas bubbles is obtained on the electrode surface during the process of multi-potential step, reconfirming its extraordinary catalytic activity towards the UOR.

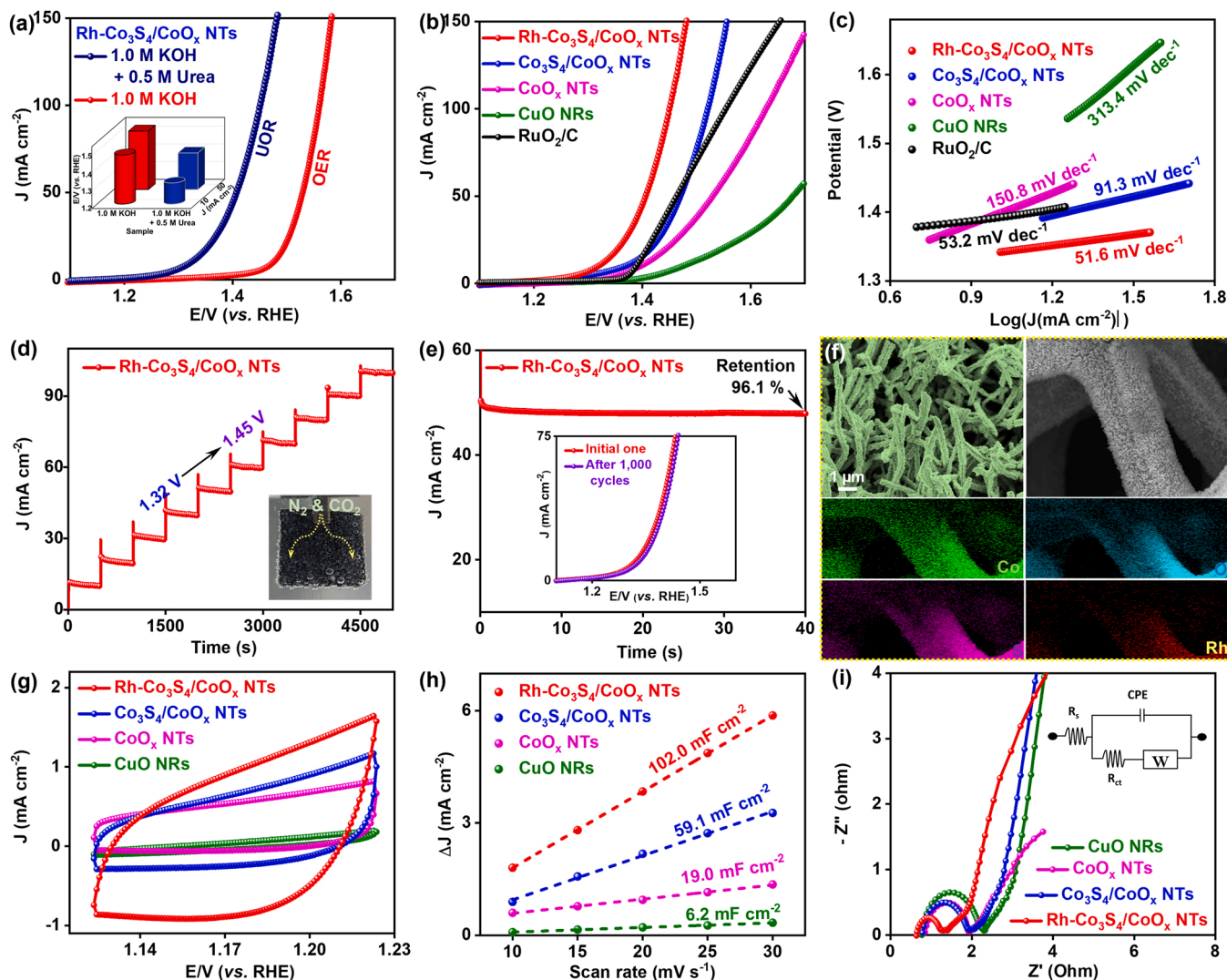


Fig. 5. Electrocatalytic activity of the as-prepared materials for the UOR in urea electrolyte (1.0 M KOH + 0.5 M urea): (a) *iR*-corrected LSV curves recorded under OER and UOR conditions of the main Rh-Co₃S₄/CoO_x NTs sample. (b) *iR*-corrected LSV curves and (c) the corresponding Tafel plots of CuO NRs, CoO_x NTs, Co₃S₄/CoO_x NTs, Rh-Co₃S₄/CoO_x NTs, and RuO₂ under UOR conditions. (d) Multi-step chronoamperometric curve of the Rh-Co₃S₄/CoO_x NTs; inset of figure d: photograph of Rh-Co₃S₄/CoO_x NTs electrode during the multi-step chronoamperometric testing. (e) Chronoamperometric curve of the Rh-Co₃S₄/CoO_x NTs; inset of figure e: LSV curves of the Rh-Co₃S₄/CoO_x NTs recorded before and after 1000 CV cycles. (f) SEM and EDS elemental mapping images of the post-UOR Rh-Co₃S₄/CoO_x NTs. (g) CV curves of Rh-Co₃S₄/CoO_x NTs, Co₃S₄/CoO_x NTs, CoO_x NTs, and CuO NRs at a scan rate of 10 mV s⁻¹. (h) The current density variation ($\Delta J = J_{\text{anode}} - J_{\text{cathode}}$) as a function of scan rates of the Rh-Co₃S₄/CoO_x NTs, Co₃S₄/CoO_x NTs, CoO_x NTs, and CuO NRs. (i) Nyquist plots of the Rh-Co₃S₄/CoO_x NTs, Co₃S₄/CoO_x NTs, CoO_x NTs, and CuO NRs; inset of i: an equivalent circuit to fit the Nyquist plots for evaluate R_{ct} and solution resistance.

Chronoamperometric analysis was next performed to further probe the electrochemical stability of Rh-Co₃S₄/CoO_x NTs sample under the condition of UOR reaction by observing the current response upon a constant potential applied to Rh-Co₃S₄/CoO_x NTs for 40 h. As expected, the Rh-Co₃S₄/CoO_x NTs suffers good stability, which shows the great maintenance of current response of 50 mA cm⁻², with only 3.9% loss of current after 40 h of continuous operation. The LSV curve after 1000 CV cycles is similar to the initial one, as shown in the inset of Fig. 5e, once again confirming the good retention of the catalytic activity of Rh-Co₃S₄/CoO_x NTs upon long-term working in urea-containing medium. The characteristics of the post-UOR Rh-Co₃S₄/CoO_x NTs after long-term stability testing were also studied by a series of analysis techniques of material. By conducting SEM, and EDS mapping analyses (Fig. 5f), the morphology, and chemical composition of the post-UOR Rh-Co₃S₄/CoO_x NTs are revealed, showing its almost unchanged morphological and chemical elemental properties, when compared to the virgin one. Like the OER process, the XRD and XPS analyses of the post-UOR Rh-Co₃S₄/CoO_x NTs also demonstrate the in situ formation of

electrocatalytically active CoOOH phase after running chronoamperometry (Fig. S9), which is attributed to the partial conversion of Co₃S₄ and Co under condition of high oxidation potential of UOR reaction and is beneficial to the enhanced UOR performance of our material [56]. Concurrently, we carried out the determination of ECSA on the basis of C_{dl} to reach further insight into the reason why the UOR activity of Rh-Co₃S₄/CoO_x NTs is better than its counterparts (Fig. 5g, h, and S10). It is not surprising that the Rh-Co₃S₄/CoO_x NTs presents a larger C_{dl} of 102.0 mF cm⁻² than those of the Co₃S₄/CoO_x NTs, CoO_x NTs, and CuO NRs of 59.1, 19.0, and 6.2 mF cm⁻², respectively. Obviously, the comparative samples without the opened structural feature of nanotube (as CuO NRs), without catalyst active Co₃S₄ component with quintessential interface (as CoO_x NTs), as well as without adjutant single Rh atoms and clusters (as Co₃S₄/CoO_x NTs), demonstrate inferior ECSA values, compared to the well-constructed Rh-Co₃S₄/CoO_x NTs. The excellent UOR behavior of the Rh-Co₃S₄/CoO_x NTs is thus plausibly associated with its unique morphological and component features, which can render the supply of more abundant catalytic active species

for the UOR. Subsequently, we also used EIS analysis to access the R_{ct} of as-prepared samples (Fig. 5i). The EIS data was fitted by using an equivalent electrical circuit (inset of Fig. 5i), which displays that the Rh-Co₃S₄/CoO_x NTs can deliver a lowest R_{ct} of about 0.63 Ω among the others (Co₃S₄/CoO_x NTs, CoO_x NTs, and CuO NRs with 1.18, 1.12, and 1.58 Ω , respectively), meaning the most favorable electron transfer within the Rh-Co₃S₄/CoO_x NTs structure during the process of UOR. This may be due to the formation of opened tubular structure and the interconnection of nanosheet assembled into the form of nanotube, which are beneficial to the exposure of more active sites, enhancement of the catalyst-electrolyte interface, and promotion of the gas release rate. Additionally, the combination of single Rh atoms/clusters can provide richly additive active centers, as well as adjust the conductive behavior of the host Co₃S₄/CoO_x, thereby improving the charge transfer ability of the entire Rh-Co₃S₄/CoO_x NTs material.

Because of the critical role of HER as a key cathodic reaction in both

water and urea electrolysis, we then turned our interest to evaluating the electrocatalytic behavior of Rh-Co₃S₄/CoO_x NTs and the other prepared samples, along with commercial Pt/C catalysts, for the HER. Fig. 6a compares the electrochemical performances of the Rh-Co₃S₄/CoO_x NTs for HER in pure 1.0 M KOH and urea-rich electrolyte (1.0 M KOH + 0.5 M urea). It is clearly evident that the LSV curve in pure electrolyte almost overlaps with that in urea-rich electrolyte. From these LSV data, the overpotentials are found to be 56.1 and 124.2 mV for Rh-Co₃S₄/CoO_x NTs in pure alkaline electrolyte to achieve current densities of 10 and 50 mA cm⁻², respectively, which are comparable to those in electrolyte with urea of 57.2 and 136.0 mV at the same current densities, suggesting its stable performance in the conditions with or without urea; or in other words, the addition of urea to electrolyte brings little effect on the HER efficiency, and therefore almost no influence on the overall urea splitting. The HER performance of Rh-Co₃S₄/CoO_x NTs in pure 1.0 M KOH also exhibits lower overpotentials at 10 and 50 mA cm⁻²,

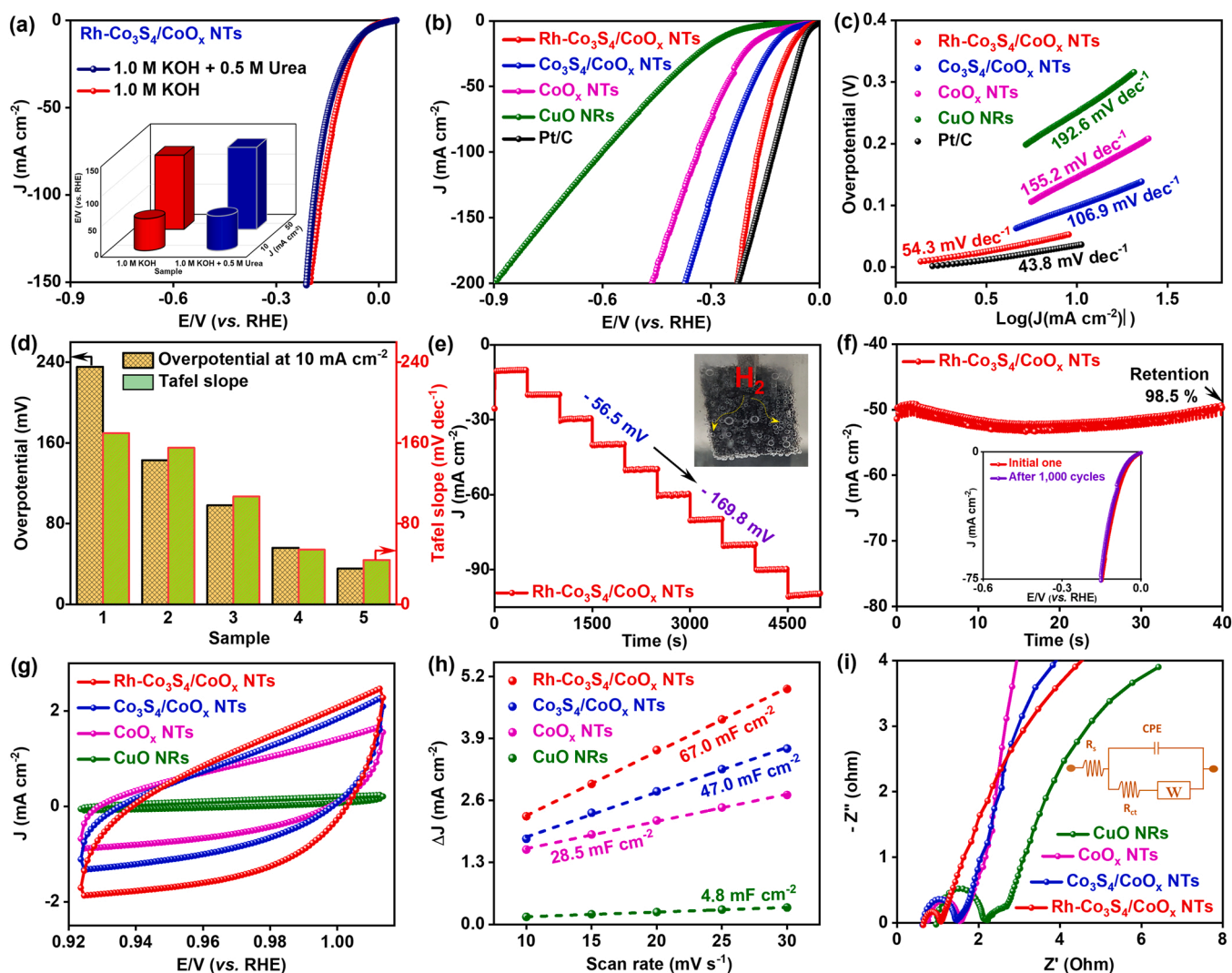


Fig. 6. Electrocatalytic activity of the as-prepared materials for the HER in alkaline conditions (1.0 M KOH): (a) *iR*-corrected LSV curves recorded under HER conditions with and without urea of the main Rh-Co₃S₄/CoO_x NTs sample; inset of a: comparison of overpotential between HER conditions with urea and HER conditions without urea. (b) *iR*-corrected LSV curves and (c) the corresponding Tafel plots of CuO NRs, Co₃S₄/CoO_x NTs, Rh-Co₃S₄/CoO_x NTs, and RuO₂ under HER conditions. (d) Comparison of overpotential and Tafel slope between the Rh-Co₃S₄/CoO_x NTs and the referenced materials ((1): CuO NRs, (2): CoO_x NTs, (3): Co₃S₄/CoO_x NTs, (4): Rh-Co₃S₄/CoO_x NTs, and (5): Pt/C). (e) Multi-step chronoamperometric curve of the Rh-Co₃S₄/CoO_x NTs; inset of figure d: photograph of Rh-Co₃S₄/CoO_x NTs electrode during the multi-step chronoamperometric testing. (f) Chronoamperometric curve of the Rh-Co₃S₄/CoO_x NTs; inset of figure e: LSV curves of the Rh-Co₃S₄/CoO_x NTs recorded before and after 1000 CV cycles. (g) CV curves of Rh-Co₃S₄/CoO_x NTs, Co₃S₄/CoO_x NTs, CoO_x NTs, and CuO NRs at a scan rate of 10 V s⁻¹. (h) The current density variation ($\Delta J = J_{\text{anode}} - J_{\text{cathodes}}$ at 0.9696 V vs. RHE) as a function of scan rates of the Rh-Co₃S₄/CoO_x NTs, Co₃S₄/CoO_x NTs, CoO_x NTs, and CuO NRs. (i) Nyquist plots of the Rh-Co₃S₄/CoO_x NTs, Co₃S₄/CoO_x NTs, CoO_x NTs, and CuO NRs; inset of i: an equivalent circuit to fit the Nyquist plots for evaluate R_{ct} and solution resistance.

when compared with the $\text{Co}_3\text{S}_4/\text{CoO}_x$ NTs, CoO_x NTs, and CuO NRs values of (98.3 and 190.4), (143.0 and 259.5), and (235.6 and 356.8) mV, respectively (Fig. 6b and d). Importantly, the HER performance of our developed catalyst is close to that of the commercial Pt/C, which is evidenced by slightly 20.8 and 44.0 mV higher the overpotentials of Pt/C at 10 and 50 mA cm^{-2} current densities, respectively. Further, when the current density increases to 170 mA cm^{-2} or higher, the Rh- $\text{Co}_3\text{S}_4/\text{CoO}_x$ NTs is comparable to the Pt/C in terms of overpotential values, indicating that its required energy input is comparable to that of commercial catalyst, as a favorable guarantee for the HER process. Moreover, the Tafel slopes of Rh- $\text{Co}_3\text{S}_4/\text{CoO}_x$ NTs and the comparative samples: $\text{Co}_3\text{S}_4/\text{CoO}_x$ NTs, CoO_x NTs, CuO NRs, and Pt/C are identified to be 54.3, 106.9, 155.2, 192.6, and 43.8 mV dec^{-1} , respectively, as depicted in Fig. 6c and d. Notably, the Rh- $\text{Co}_3\text{S}_4/\text{CoO}_x$ NTs shows less Tafel slope value than its counterparts, suggesting its excellent reaction dynamic for HER; the Tafel slope of Rh- $\text{Co}_3\text{S}_4/\text{CoO}_x$ NTs also approaches that of Pt/C, confirming its Pt-like hydrogen evolution kinetics. At the same time, the comparison in Table S3 shows that the catalytic activity of the Rh- $\text{Co}_3\text{S}_4/\text{CoO}_x$ NTs is comparable with, and even better than those of the recently reported HER catalysts in the literature, corroborating its excellent performance. In addition to the catalytic activity, stability has been considered as an essential indicator to evaluate the commercialization capacity and competitiveness of the HER electrocatalysts for practical applications. When operating the HER at different overpotentials, the current response of Rh- $\text{Co}_3\text{S}_4/\text{CoO}_x$ NTs at each applied potential remains stable during a 500 s measurement throughout all 5000 s testing, suggesting the excellent mass transfer, as well as stability, of the Rh- $\text{Co}_3\text{S}_4/\text{CoO}_x$ NTs (Fig. 6e). The rich profusion of H_2 bubbles on the surface of Rh- $\text{Co}_3\text{S}_4/\text{CoO}_x$ NTs electrode during multi-potential step testing (inset of Fig. 6e) is additional evidence for its superior HER efficiency. By maintaining the applied overpotential of 124.2 mV vs. RHE, the response of current density in Fig. 6f shows that it can be retained with a negligible degradation of 1.5% after 40 h testing for the Rh- $\text{Co}_3\text{S}_4/\text{CoO}_x$ NTs electrode. Further, the LSV curve after 1000 CV cycles seem to be almost unchanged compared to the initial one (inset of Fig. 6f), reconfirming the almost unchanged HER behavior. Regarding the post-HER Rh- $\text{Co}_3\text{S}_4/\text{CoO}_x$ NTs after chronoamperometric testing, the morphological features are retained, as shown in Fig. S11a and b, and the corresponding EDS mapping images also reveal the homogeneous distribution of Rh, Co, O, and S (Figs. S11c-f). The XRD pattern and XPS spectra in Fig. S12 exhibit all the characteristic signals of the Rh- $\text{Co}_3\text{S}_4/\text{CoO}_x$ NTs material, corroborating its good structural stability under the harsh HER conditions. The ECSA for HER condition was also determined based on the basic electrochemical C_{dl} (Figs. S13, 6g and h). The measured C_{dl} of Rh- $\text{Co}_3\text{S}_4/\text{CoO}_x$ NTs is 67.0 mF cm^{-2} , showing 20.0, 38.5, and 62.2 mF cm^{-2} increase when compared to the $\text{Co}_3\text{S}_4/\text{CoO}_x$ NTs, CoO_x NTs, and CuO NRs, respectively, indicating the significantly improved ECSA of the Rh- $\text{Co}_3\text{S}_4/\text{CoO}_x$ NTs. This result reflects the exposure of more accessible active sites for reaction within its structure than in the counterparts, which is considered as one of the key factors for the well-designed structure to increase HER performance. In addition, the EIS in Fig. 6i shows that the Rh- $\text{Co}_3\text{S}_4/\text{CoO}_x$ NTs has a much lower R_{ct} of 0.41 Ω than the others of $\text{Co}_3\text{S}_4/\text{CoO}_x$ NTs, CoO_x NTs, and CuO NRs of 0.81, 0.78, and 1.19, respectively, revealing its best capacity for electron and mass transfer compared to the others, and thus leading to accelerated kinetics for the HER reaction.

To elucidate the influence of S content on the catalytic activity of Rh- $\text{Co}_3\text{S}_4/\text{CoO}_x$ NTs, the comparative samples named as Rh- $\text{Co}_3\text{S}_4/\text{CoO}_x$ NTs-1 and Rh- $\text{Co}_3\text{S}_4/\text{CoO}_x$ NTs-2 were synthesized by reducing (0.005 M Na_2S) and enhancing (0.02 M Na_2S) the amount of sulfur-salt precursor, respectively, to change the S content. The OER, UOR, and HER performances of these samples were tested by LSV and Tafel plot measurements and provided in Fig. S14. Obviously, when reducing the S content, the overpotentials at current density of 10 mA cm^{-2} of OER and HER are raised, up to 279.1, and 106.4 mV, respectively. The potential at current density of 10 mA cm^{-2} of UOR is also higher as reduced the S

content. Similarly, upon increasing the S content, the overpotentials of OER and HER, as well as potential of UOR are also negligible alteration. The overpotentials of OER and HER at current density of 10 mA cm^{-2} of Rh- $\text{Co}_3\text{S}_4/\text{CoO}_x$ NTs-2 are 22.6 and 43.2 mV higher than those of the Rh- $\text{Co}_3\text{S}_4/\text{CoO}_x$ NTs, respectively. The potential of UOR at current density of 10 mA cm^{-2} of Rh- $\text{Co}_3\text{S}_4/\text{CoO}_x$ NTs-2 is also 7 mV higher than that of the Rh- $\text{Co}_3\text{S}_4/\text{CoO}_x$ NTs. Thus, the catalytic performances of both Rh- $\text{Co}_3\text{S}_4/\text{CoO}_x$ NTs-1 and Rh- $\text{Co}_3\text{S}_4/\text{CoO}_x$ NTs-2 are slight degradation as compared to the Rh- $\text{Co}_3\text{S}_4/\text{CoO}_x$ NTs. Tafel plots also show the inferior capabilities of Rh- $\text{Co}_3\text{S}_4/\text{CoO}_x$ NTs-1 and Rh- $\text{Co}_3\text{S}_4/\text{CoO}_x$ NTs-2 in boosting reaction kinetics to the Rh- $\text{Co}_3\text{S}_4/\text{CoO}_x$ NTs. Consequently, the Rh- $\text{Co}_3\text{S}_4/\text{CoO}_x$ NTs with 0.01 M Na_2S is considered to provide optimal catalytic behavior for the OER, UOR, and HER in comparison to the others. The results also confirm the essential role of cobalt sulfide, which provides catalytically active sites and a highly efficient avenue for quickly charge transfer, in improving catalytic activity of the entire Rh- $\text{Co}_3\text{S}_4/\text{CoO}_x$ NTs material.

Based on the extraordinary electrocatalytic activity and stability of Rh- $\text{Co}_3\text{S}_4/\text{CoO}_x$ NTs for both OER and HER, we thus successfully developed a water splitting device containing Rh- $\text{Co}_3\text{S}_4/\text{CoO}_x$ NTs as both cathode and anode in two-electrode configuration (Fig. 7a). The optical images of electrode surface in the inset of Fig. 7a show that during the process of electrocatalysis, large numbers of O_2 and H_2 bubbles can be identified on the Rh- $\text{Co}_3\text{S}_4/\text{CoO}_x$ NTs anode and cathode, respectively, suggesting the desirable efficiency of the developed device. A reference device was also constructed by using the benchmark precious Pt/C and RuO_2 catalysts as cathode and anode, respectively. As represented in Fig. 7b, the Rh- $\text{Co}_3\text{S}_4/\text{CoO}_x$ NTs (+, -)-based electrolyzer shows remarkable performance, gaining current densities of 10 and 50 mA cm^{-2} at small applied cell voltages of 1.45 and 1.57 V, respectively, which are slightly higher than those of Pt/C (+) // RuO_2 (-)-based electrolyzer of 1.40 and 1.52 V (Fig. 7c). These cell voltage values are also superior to those of most of the bifunctional electrocatalysts in the very recent literature, as compared in Fig. 7d. Further, we evaluated the FE for both HER and OER during electrolysis to fully understand the utilization efficiency of electrons that participate in this process [57]. The plots in Fig. 7e demonstrate the good agreement between the evolved gas amounts with those of the theoretical values. The generation of gaseous species obeys a volume ratio of 2: 1, wherein 2 reflects the volume of the generated H_2 and 1 the volume of generated oxygen, confirming the full conversion of water into these gases. In fact, the FE is found to be around 99.7% and 99.5% for the HER and OER, respectively. Such close to 100% FE values for HER and OER once again prove the excellent catalytic performance of the Rh- $\text{Co}_3\text{S}_4/\text{CoO}_x$ NTs, and its expected prospect for industrial applications. During the long-term stability testing realized at an applied potential of 1.57 V vs. RHE (Fig. 7h), 92.5% current density was retained after 50 h testing. Further, the comparison of LSV curve and cell voltages after stability with the initial ones in the inset of Fig. 7h displays that the cell voltages of Rh- $\text{Co}_3\text{S}_4/\text{CoO}_x$ NTs reveal little fluctuation during 50 h continuous running, confirming its robustness under a water electrolysis environment.

The Rh- $\text{Co}_3\text{S}_4/\text{CoO}_x$ NTs also presents excellent catalytic properties for the HER and UOR, as compared in Fig. 8a, which is strong motivation for designing a urea electrolyzer by using Rh- $\text{Co}_3\text{S}_4/\text{CoO}_x$ NTs materials as both cathodic and anodic electrodes in a two-electrode system, towards closely approaching practical applications. The comparison between urea electrolysis performance and water electrolysis performance upon the action of Rh- $\text{Co}_3\text{S}_4/\text{CoO}_x$ NTs in Fig. 8b shows the remarkable advantages the urea electrolysis has of overall water electrolysis in terms of the thermodynamic and catalytic kinetics. The Rh- $\text{Co}_3\text{S}_4/\text{CoO}_x$ NTs (+, -)-based urea electrolyzer can derive current densities of 10 and 50 mA cm^{-2} at low applied cell voltages of 1.35 and 1.48 V, respectively. Interestingly, to achieve a much higher current density of 100 mA cm^{-2} , the electrolyzer also requires a cell voltage of merely 1.54 V. These cell voltage values of urea electrolyzer are much lower, when compared to that of the Rh- $\text{Co}_3\text{S}_4/\text{CoO}_x$ NTs (+, -)-based water

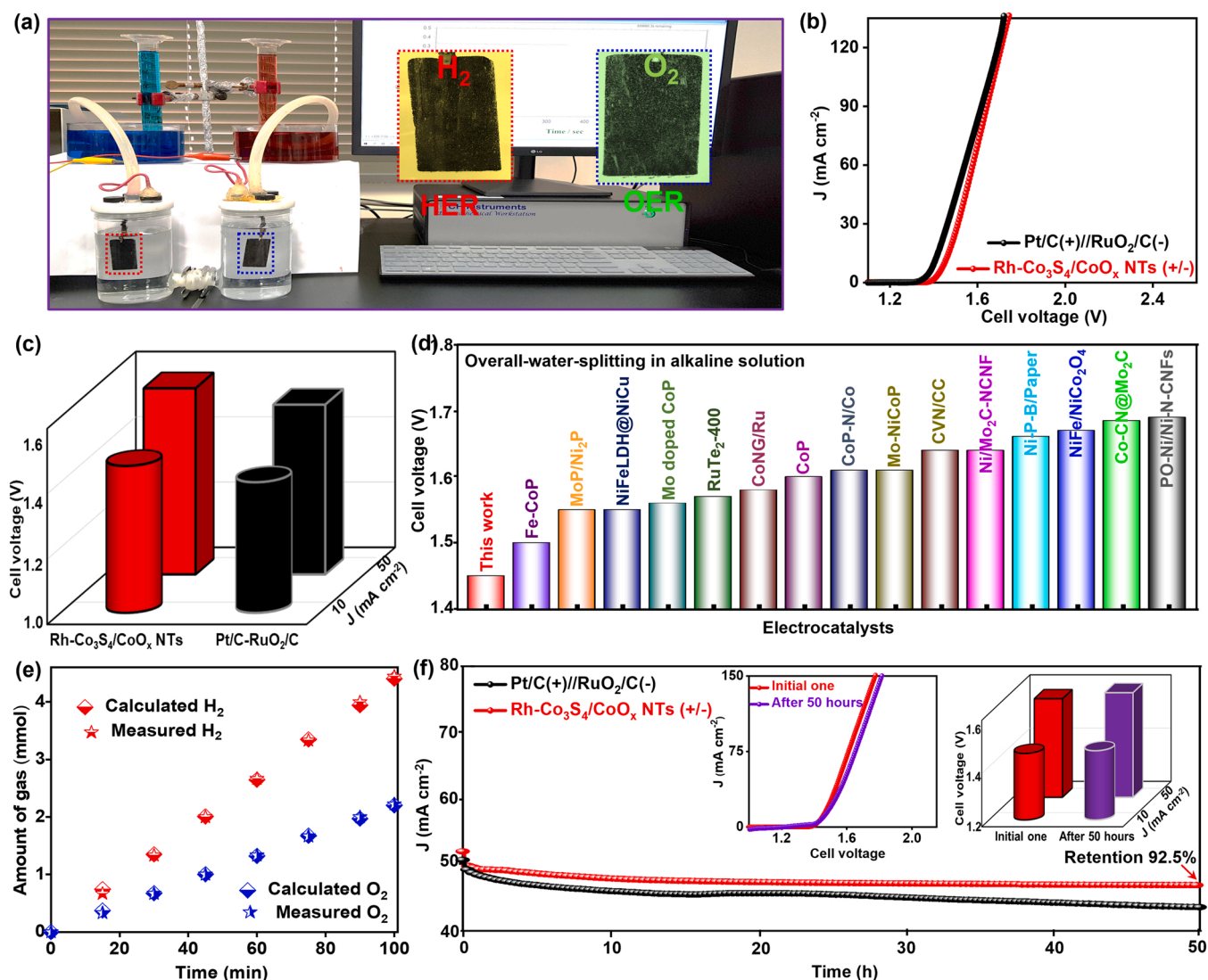


Fig. 7. Electrocatalytic activity of the as-prepared materials for overall water splitting: (a) photograph of electrolyzer assembled by Rh-Co₃S₄/CoO_x NTs as both cathode and anode. (b) LSV curves of Rh-Co₃S₄/CoO_x NTs (+, -) and Pt (+) // RuO₂ (-) electrolyzer. (c) Comparison of cell voltages at 10 and 50 mA cm⁻² between Rh-Co₃S₄/CoO_x NTs (+, -) and Pt (+) // RuO₂ (-) electrolyzer. (d) Comparison of cell voltages at 10 mA cm⁻² between of Rh-Co₃S₄/CoO_x NTs (+, -) and other bifunctional electrocatalysts reported elsewhere. (e) Experimental and theoretical gas volume versus time for the HER and OER process. (f) Chronoamperometric curve of the Rh-Co₃S₄/CoO_x NTs (+, -); inset of figure f: LSV curves and cell voltages of the Rh-Co₃S₄/CoO_x NTs recorded before and after chronoamperometric testing.

electrolyzer (Fig. 8c). More importantly, the performance of full urea electrolysis using our catalyst is superior to that of the urea electrolyzer using the commercial Pt/C and RuO₂ catalysts as electrode material, which is demonstrated by 30 and 30 mV higher cell voltage compared to that of our material at 10 and 50 mA cm⁻², respectively (Fig. 8d and e). Such small cell voltages of the Rh-Co₃S₄/CoO_x NTs both suggest its desirable urea electrolysis capability, even at high current densities, and reflect its promising potential for real applications. The performance of urea electrolysis based on the Rh-Co₃S₄/CoO_x NTs catalysts also outperforms most of the recently reported bifunctional electrocatalysts in the literature (Fig. 8f). The chronoamperometric curve in Fig. 8g recorded at a constant potential of 1.48 V vs. RHE confirms the high stability and durability of the Rh-Co₃S₄/CoO_x NTs under full urea electrolysis conditions, as the retention of current density response is very high, at about 98.5% after 50 h of continuous electrolysis. Moreover, the LSV recorded after stability testing and cell voltages (inset of Fig. 8g) seems to be similar to the initial one; this is favorable evidence for the long lifetime of the Rh-Co₃S₄/CoO_x NTs without significant deactivation. During the process of chronoamperometric testing,

numerous gas bubbles are continuously formed on the surface of both cathode and anode via the HER and UOR, respectively, as seen in Fig. 8h, reconfirming that our catalyst is a good candidate for urea electrolysis towards enhanced urea-rich wastewater treatment and energy-saving H₂ production.

Aside from the high electrical conductivity and large ECSA discussed above for OER, UOR, and HER, good hydrophilicity is also an important behavior of electrocatalysts, because the super-hydrophilic surface can endow the electrodes with fast reaction kinetics and superior catalytic behavior. We evaluated the wettability of the developed catalysts by measuring the dynamic electrolyte contact angle. Fig. 9a depict the dynamic electrolyte contact angle changes versus time of the bare 3D-CF and the Rh-Co₃S₄/CoO_x NTs. It can clearly be seen that the pure 3D-CF samples show rather low hydrophilicity behavior, as they exhibit initial contact angles of 90° and mostly maintain contact angles of 72° for 10 s or longer. By contrast, the contact angle of the Rh-Co₃S₄/CoO_x NTs appears to be 0° at the beginning, proving the super-hydrophilic surface of our material. The Rh-Co₃S₄/CoO_x NTs with super-hydrophilic surface may have an easier infiltration process of electrolyte into their internal

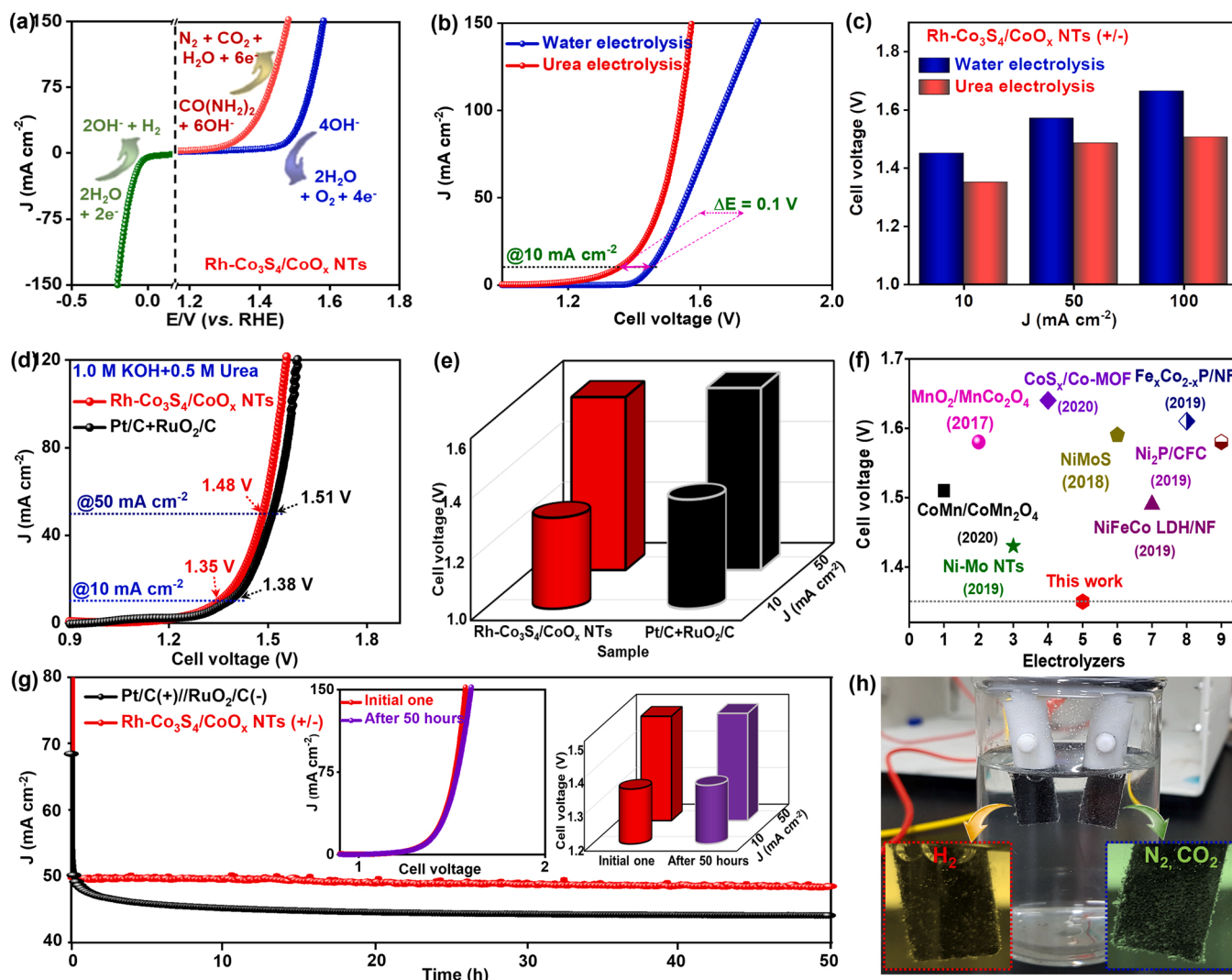


Fig. 8. Electrocatalytic activity of the as-prepared materials for full urea electrolysis: (a) Comparison of electrochemical properties of the Rh-Co₃S₄/CoO_x NTs for UOR, OER, and HER. (b) LSV curves recorded under urea and water electrolysis of the main Rh-Co₃S₄/CoO_x NTs sample. (c) Comparison of cell voltages at 10 and 50 mA cm⁻² of Rh-Co₃S₄/CoO_x NTs between urea electrolysis and water electrolysis. (d) LSV curves of Rh-Co₃S₄/CoO_x NTs (+, -) and Pt (+) // RuO₂ (-) electrolyzer under urea electrolysis. (e) Comparison of cell voltages at 10 and 50 mA cm⁻² between Rh-Co₃S₄/CoO_x NTs (+, -) and Pt (+) // RuO₂ (-) electrolyzer under urea electrolysis. (f) Comparison of cell voltages at 10 mA cm⁻² between Rh-Co₃S₄/CoO_x NTs (+, -) and other bifunctional electrocatalysts for urea electrolysis reported elsewhere. (g) Chronoamperometric curve of the Rh-Co₃S₄/CoO_x NTs (+, -) under urea electrolysis; inset of figure f: LSV curves and cell voltages of the Rh-Co₃S₄/CoO_x NTs recorded before and after chronoamperometric testing. (h) photograph of cathodic and anodic Rh-Co₃S₄/CoO_x NTs electrodes during the urea electrolysis.

places than that of the hydrophobic 3D-CF framework, leading to facilitating the contact between internal active sites and reactant/electrolyte molecules, and thereby increasing the density of accessible active sites [58]. In the formation of Co₃S₄ and CoO, the introduction of isolated Rh atomic single sites, and the morphological feature of nanotube array, the wettability of Rh-Co₃S₄/CoO_x NTs is superior to that of the bare 3D-CF. This is because both Co₃S₄ and CoO are semiconductors that have a very high capability for the adsorption of hydroxyl species. It is well known that the material with high density of hydroxyl groups on its surface possesses a hydrophilic surface, which can be attributed to the hydrophilic nature of hydroxyl groups in promoting the penetration of water drop through a 3D capillary effect [59,60]. In addition, the formation of additive polar Rh-O bond via the anchorage of Rh on the Co₃S₄/CoO_x surface, together with the intrinsic hydrophilic character of 3D nanotube array structure, are additional reasons for the super-hydrophilic property of the Rh-Co₃S₄/CoO_x NTs sample [61]. This result serves as additive evidence for the good catalytic activity for electrochemical reactions of Rh-Co₃S₄/CoO_x NTs.

To explore the reason for very efficient catalytic process upon the

action of adjunct Rh, as well as the synergy of metal sulfide and metal oxide within the developed structure, density functional theory (DFT) calculations were performed, in addition to the characterizations discussed above. Fig. 9b and e show the model of two systems that include the metal sulfide/oxide materials without and with Rh, such as (CoO, Co₃S₄, and Co₃S₄/CoO) and (Rh-CoO, Rh-Co₃S₄, and Rh-Co₃S₄/CoO), respectively. As demonstrated above, upon the introduction of Rh, as well as the combination of Co₃S₄ and CoO, the ρ_{ct} values of the entire material are reduced, which is closely related to the significant improvement of catalyst conductivity. As can be seen in Fig. 9c and f, the calculated density of states (DOS) of all (CoO, Co₃S₄, and Co₃S₄/CoO) and (Rh-CoO, Rh-Co₃S₄, and Rh-Co₃S₄/CoO) systems emerge around the Fermi level, indicating the intrinsic metallic nature of these catalysts [62]. Importantly, the Rh-Co₃S₄/CoO exhibits obviously enhanced DOS near the Fermi level relative to the other comparative catalysts, suggesting that its electrical property is significantly improved by the assistance of the foreign Rh and the synergistic effect of the cobalt sulfide/oxide heterostructure [63]. The Rh-Co₃S₄/CoO with excellent electrical behavior can provide both a larger amount of charge carriers

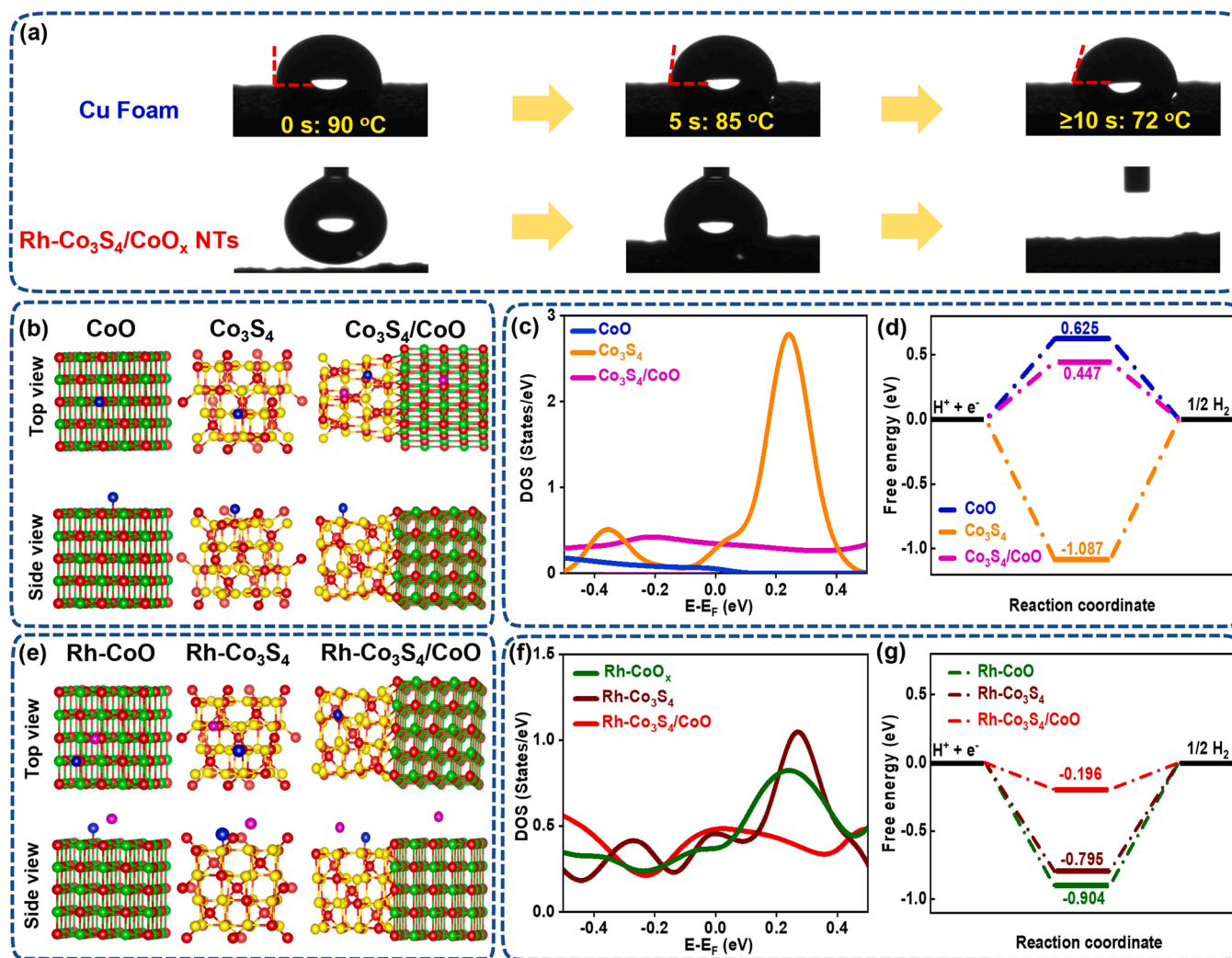


Fig. 9. (a) Dynamic electrolyte contact angle measurement for bare 3D-CF, and Rh-Co₃S₄/CoO_x NTs. DFT calculations: (b) and (e) The model of two systems included (CoO, Co₃S₄, Co₃S₄/CoO) and (Rh-CoO, Rh-Co₃S₄, Rh-Co₃S₄/CoO), respectively (the red, green, yellow, orange, blue balls are Co, O, S, Rh, and H, respectively); (c) and (f) Calculated density of states for (CoO, Co₃S₄, Co₃S₄/CoO) and (Rh-CoO, Rh-Co₃S₄, Rh-Co₃S₄/CoO), respectively; (d) and (g) The DFT calculated hydrogen adsorption free energy diagram of (CoO, Co₃S₄, Co₃S₄/CoO) and (Rh-CoO, Rh-Co₃S₄, Rh-Co₃S₄/CoO), respectively.

for electrochemical reactions, and a superior electrical conductivity to boost the process of electron transfer, promising the remarkable improvement of OER, UOR, and HER catalytic efficiencies [64]. In addition to DOS, the Gibbs free energy change is also recognized as one of the most important criteria in evaluating the basic activity of the catalysts. Accordingly, the DFT calculations were also used to evaluate the HER Gibbs free energy change (ΔG_{H^*}) in an alkaline environment for the above systems. Fig. 9d and g present the ΔG_{H^*} diagrams of the (CoO, Co₃S₄, and Co₃S₄/CoO) and (Rh-CoO, Rh-Co₃S₄, and Rh-Co₃S₄/CoO) systems, respectively. It is obvious that ΔG_{H^*} is 0.625 and -1.087 eV for the CoO, and Co₃S₄ alone, while the combination of these components closes the ΔG_{H^*} of Co₃S₄/CoO to the ideal value of ΔG_{H^*} (0 eV), up to 0.447 eV, confirming the better capacity of the heterostructured Co₃S₄/CoO for H intermediate adsorption, with respect to that of the others (Fig. 9d). Moreover, the integration of adjutant Rh also changes the ΔG_{H^*} , up to -0.904, -0.795, and -0.196 eV in the Rh-CoO, Rh-Co₃S₄, and Rh-Co₃S₄/CoO, respectively (Fig. 9g). In contrast to the comparative catalysts, Rh-Co₃S₄/CoO possesses ΔG_{H^*} value closest to zero, meaning its ability for H adsorption is the most moderate among the others, which is of great significance to the efficiency of the H adsorption/desorption process during the process of HER, and finally increases the HER performance towards increasing the full water/urea electrolysis performance.

Overall, the extraordinary catalytic property and durability of Rh-Co₃S₄/CoO_x NTs for water splitting and urea electrolysis can be assigned to the following aspects. (1) The uniform assembly of Co₃S₄/CoO_x NSs into 1D nanotubes supplies a large amount of accessibly active sites for intermediates, as well as restricting the aggregation tendency of active materials during catalysis process. Thus, the Rh-Co₃S₄/CoO_x NTs can achieve high current densities at very low overpotentials and potentials, which outperform previous precious-free electrocatalysts for all HER, OER, and UOR. (2) The tubular characteristic can enlarge the surface-volume ratio toward facilitating the contact between active centers and reactants, while the 1D structure can promote electron/mass transfer. Consequently, the Rh-Co₃S₄/CoO_x NTs presents a larger ECSA, as well as a lower R_{ct} , than those of its counterpart. (3) The design of Rh in the form of single atoms and subnanometer clusters can effectively reduce the amount of Rh used, thereby largely contributing to minimizing the cost of electrocatalysts, however, while still increasing the utilization rate of Rh, as a precious group metal. (4) The electronic interaction between adjustable Rh and host Co species may redistribute the electronic density of both Rh and Co, facilitating the interaction between them and intermediate species during electrolysis, and thus leading to significantly improved electrocatalytic kinetics, as demonstrated by the DFT calculations. (5) The vertically ultrathin Co₃S₄/CoO_x NSs-assembled NTs can supply large open space and efficient paths to

promote the mass and charge transport, respectively, as well as accelerating gas release to ensure an always free critical solid-liquid interface. (6) The in situ growth of catalytic material on framework favors its strong adhesion, which is beneficial to electron transfer and mechanical stability, while the highly-conductive 3D foam plays a support role in further improving the charge transfer ability of the entire catalyst.

4. Conclusions

In summary, the proposed Rh-Co₃S₄/CoO_x NTs electrocatalyst possesses excellent characteristics in view of its morphological structure and electronic density, which endow the catalysts with superior electrocatalytic behavior for OER, UOR, and HER towards full water and urea electrolysis. Introduction of Rh improves the electrolysis efficiency and promotes the reaction kinetics, which are beneficial to catalytic performance. While the other advantages, including tubular feature, synergy of Rh and Co, 3D structure, and self-standing property also play dominant role in improving catalytic performance. The as-synthesized catalyst also exhibits superior catalytic activity and stability at high current density, therefore showing great capability in practical applications toward industrial scale production of hydrogen fuel by green and energy-saving approaches.

CRediT authorship contribution statement

Dinh Chuong Nguyen: Conceptualization, Methodology, Writing – original draft, Validation, Visualization. **Thi Luu Luyen Doan:** Methodology, Investigation, Formal analysis, Writing – review & editing. **Mr. Sampath Prabhakaran:** Density-functional theory calculation. **Do Hwan Kim:** Density-functional theory calculation, Writing – review & editing. **Nam Hoon Kim:** Conceptualization, Data curation, Writing – review & editing, Supervision. **Joong Hee Lee:** Conceptualization, Writing – review & editing, Supervision, Project administration.

Declaration of Competing Interest

The authors declare that they have no known competing financial interests or personal relationships that could have appeared to influence the work reported in this paper.

Acknowledgments

This research was supported by the Basic Science Research Program (2019R1A2C1004983) and the Regional Leading Research Center Program (2019R1A5A8080326) through the National Research Foundation funded by the Ministry of Science and ICT of Republic of Korea.

Appendix A. Supporting information

Supplementary data associated with this article can be found in the online version at [doi:10.1016/j.apcatb.2022.121430](https://doi.org/10.1016/j.apcatb.2022.121430).

References

- T.L.L. Doan, D.C. Nguyen, S. Prabhakaran, D.H. Kim, D.T. Tran, N.H. Kim, J.H. Lee, Single-atom co-decorated MoS₂ nanosheets assembled on metal nitride nanorod arrays as an efficient bifunctional electrocatalyst for pH-universal water splitting, *Adv. Funct. Mater.* 31 (2021) 2100233, <https://doi.org/10.1002/adfm.202100233>.
- H. Sun, W. Zhang, J.G. Li, Z. Li, X. Ao, K.H. Xue, K.K. Ostrikov, J. Tang, C. Wang, Rh-engineered ultrathin NiFe-LDH nanosheets enable highly-efficient overall water splitting and urea electrolysis, *Appl. Catal. B Environ.* 284 (2021), 119740, <https://doi.org/10.1016/j.apcatb.2020.119740>.
- N. Mahmood, Y. Yao, J.W. Zhang, L. Pan, X. Zhang, J.J. Zou, Electrocatalysts for hydrogen evolution in alkaline electrolytes: mechanisms, challenges, and prospective solutions, *Adv. Sci.* 5 (2018) 1700464, <https://doi.org/10.1002/advs.201700464>.
- C. Wang, H. Lu, Z. Mao, C. Yan, G. Shen, X. Wang, Bimetal schottky heterojunction boosting energy-saving hydrogen production from alkaline water via urea electrocatalysis, *Adv. Funct. Mater.* 30 (2020) 2000556, <https://doi.org/10.1002/adfm.202000556>.
- J.-Y. Zhang, T. He, M. Wang, R. Qi, Y. Yan, Z. Dong, H. Liu, H. Wang, B.Y. Xia, Energy-saving hydrogen production coupling urea oxidation over a bifunctional nickel-molybdenum nanotube array, *Nano Energy* 60 (2019) 894–902, <https://doi.org/10.1016/j.nanoen.2019.04.035>.
- D.C. Nguyen, T.L. Luyen Doan, S. Prabhakaran, D.T. Tran, D.H. Kim, J.H. Lee, N. H. Kim, Hierarchical Co and Nb dual-doped MoS₂ nanosheets shelled micro-TiO₂ hollow spheres as effective multifunctional electrocatalysts for HER, OER, and ORR, *Nano Energy* 82 (2021), 105750, <https://doi.org/10.1016/j.nanoen.2021.105750>.
- G. Ma, Q. Xue, J. Zhu, X. Zhang, X. Wang, H. Yao, G. Zhou, Y. Chen, Ultrafine Rh nanocrystals decorated ultrathin NiO nanosheets for urea electro-oxidation, *Appl. Catal. B Environ.* 265 (2020), 118567, <https://doi.org/10.1016/j.apcatb.2019.118567>.
- T.L.L. Doan, D.T. Tran, D.C. Nguyen, D.H. Kim, N.H. Kim, J.H. Lee, Rational engineering Co_xO_y nanosheets via phosphorous and sulfur dual-coupling for enhancing water splitting and Zn-air battery, *Adv. Funct. Mater.* 31 (2021) 2007822, <https://doi.org/10.1002/adfm.202007822>.
- D.C. Nguyen, D.T. Tran, T.L.L. Doan, D.H. Kim, N.H. Kim, J.H. Lee, Rational design of core@shell structured CoS_x@Cu₂MoS₄ hybridized MoS₂/N,S-codoped graphene as advanced electrocatalyst for water splitting and Zn-Air battery, *Adv. Energy Mater.* 10 (2020) 1903289, <https://doi.org/10.1002/aenm.201903289>.
- X. Wang, J. Wang, X. Sun, S. Wei, L. Cui, W. Yang, J. Liu, Hierarchical coral-like NiMoS nanohybrids as highly efficient bifunctional electrocatalysts for overall urea electrolysis, *Nano Res* 11 (2018) 988–996, <https://doi.org/10.1007/s12274-017-1711-3>.
- H.L. Meng, S.Y. Lin, J.J. Feng, L. Zhang, A.J. Wang, Coordination regulated pyrolysis synthesis of ultrafine FeNi/(FeNi)₉S₈ nanoclusters/nitrogen, sulfur-codoped graphitic carbon nanosheets as efficient bifunctional oxygen electrocatalysts, *J. Colloid Interface Sci.* 610 (2022) 573–582, <https://doi.org/10.1016/j.jcis.2021.11.101>.
- R.-M. Sun, L. Zhang, J.J. Feng, K.M. Fang, A.J. Wang, In situ produced Co₉S₈ nanoclusters/Co/Mn-S, N multi-doped 3D porous carbon derived from eriochrome black T as an effective bifunctional oxygen electrocatalyst for rechargeable Zn-air batteries, *J. Colloid Interface Sci.* 608 (2022) 2100–2110, <https://doi.org/10.1016/j.jcis.2021.10.144>.
- S.Y. Lin, Y.P. Chen, Y. Cao, L. Zhang, J.J. Feng, A.J. Wang, Aminouracil-assisted synthesis of CoFe decorated bougainvillea-like N-doped carbon nanoflowers for boosting Zn-air battery and water electrolysis, *J. Power Sources* 521 (2022), 230926, <https://doi.org/10.1016/j.jpowsour.2021.230926>.
- M.T. Chen, J.J. Duan, J.J. Feng, L.P. Mei, Y. Jiao, L. Zhang, A.J. Wang, Iron, rhodium-codoped Ni₂P nanosheets arrays supported on nickel foam as an efficient bifunctional electrocatalyst for overall water splitting, *J. Colloid Interface Sci.* 605 (2022) 888–896, <https://doi.org/10.1016/j.jcis.2021.07.101>.
- S. Peng, L. Li, X. Han, W. Sun, M. Srinivasan, S.G. Mhaisalkar, F. Cheng, Q. Yan, J. Chen, S. Ramakrishna, Cobalt sulfide nanosheet/graphene/carbon nanotube nanocomposites as flexible electrodes for hydrogen evolution, *Angew. Chem.* 126 (2014) 12802–12807, <https://doi.org/10.1002/ange.201408876>.
- S. Luo, K. Wang, J. Wang, K. Jiang, Q. Li, S. Fan, Binder-free LiCoO₂/carbon nanotube cathodes for high-performance lithium ion batteries, *Adv. Mater.* 24 (2012) 2294–2298, <https://doi.org/10.1002/adma.201104720>.
- Q. Shi, C. Zhu, D. Du, J. Wang, H. Xia, M.H. Engelhard, S. Feng, Y. Lin, Ultrathin dendritic IrTe nanotubes for an efficient oxygen evolution reaction in a wide pH range, *J. Mater. Chem. A* 6 (2018) 8855–8859, <https://doi.org/10.1039/C8TA01288A>.
- K. Yu, X. Pan, G. Zhang, X. Liao, X. Zhou, M. Yan, L. Xu, L. Mai, Nanowires in energy storage devices: structures, synthesis, and applications, *Adv. Energy Mater.* 8 (2018) 1802369, <https://doi.org/10.1002/aenm.201802369>.
- P. Thangasamy, S. Oh, S. Nam, H. Randriamahazaka, I. Oh, Ferrocene-incorporated cobalt sulfide nanoarchitecture for superior oxygen evolution reaction, *Small* 16 (2020) 2001665, <https://doi.org/10.1002/smll.202001665>.
- Y. Guo, T. Park, J.W. Yi, J. Henzie, J. Kim, Z. Wang, B. Jiang, Y. Bando, Y. Sugahara, J. Tang, Y. Yamauchi, Nanoarchitectonics for transition-metal-sulfide-based electrocatalysts for water splitting, *Adv. Mater.* 31 (2019) 1807134, <https://doi.org/10.1002/adma.201807134>.
- X. Wang, Y. He, X. Han, J. Zhao, L. Li, J. Zhang, C. Zhong, Y. Deng, W. Hu, Engineering cobalt sulfide/oxide heterostructure with atomically mixed interfaces for synergistic electrocatalytic water splitting, *Nano Res* (2021), <https://doi.org/10.1007/s12274-021-3632-4>.
- X. Han, X. Wu, Y. Deng, J. Liu, J. Lu, C. Zhong, W. Hu, Ultrafine Pt nanoparticle-decorated pyrite-type CoS₂ nanosheet arrays coated on carbon cloth as a bifunctional electrode for overall water splitting, *Adv. Energy Mater.* 8 (2018) 1800935, <https://doi.org/10.1002/aenm.201800935>.
- J. Wang, W. Fang, Y. Hu, Y. Zhang, J. Dang, Y. Wu, B. Chen, H. Zhao, Z. Li, Single atom Ru doping 2H-MoS₂ as highly efficient hydrogen evolution reaction electrocatalyst in a wide pH range, *Appl. Catal. B Environ.* 298 (2021), 120490, <https://doi.org/10.1016/j.apcatb.2021.120490>.
- H. Xu, Y. Liao, Z. Gao, Y. Qing, Y. Wu, L. Xia, A branch-like Mo-doped Ni₃S₂ nanoforest as a high-efficiency and durable catalyst for overall urea electrolysis, *J. Mater. Chem. A* 9 (2021) 3418–3426, <https://doi.org/10.1039/D0TA09423D>.
- D. Guo, J. Wang, L. Zhang, X. Chen, Z. Wan, B. Xi, Strategic atomic layer deposition and electrospinning of cobalt sulfide/nitride composite as efficient bifunctional electrocatalysts for overall water splitting, *Small* 16 (2020) 2002432, <https://doi.org/10.1002/smll.202002432>.

- [26] S. Wang, X. Yang, Z. Liu, D. Yang, L. Feng, Efficient nanointerface hybridization in a nickel/cobalt oxide nanorod bundle structure for urea electrolysis, *Nanoscale* 12 (2020) 10827–10833, <https://doi.org/10.1039/D0NR01386B>.
- [27] B. Zhang, C. Zhu, Z. Wu, E. Stavitski, Y.H. Lui, T.-H. Kim, H. Liu, L. Huang, X. Luan, L. Zhou, K. Jiang, W. Huang, S. Hu, H. Wang, J.S. Francisco, Integrating Rh Species with NiFe-layered double hydroxide for overall water splitting, *Nano Lett.* 20 (2020) 136–144, <https://doi.org/10.1021/acs.nanolett.9b03460>.
- [28] T.L. Luyen Doan, D.T. Tran, D.C. Nguyen, H. Tuan Le, N.H. Kim, J.H. Lee, Hierarchical three-dimensional framework interface assembled from oxygen-doped cobalt phosphide layer-shelled metal nanowires for efficient electrocatalytic water splitting, *Appl. Catal. B Environ.* 261 (2020), 118268, <https://doi.org/10.1016/j.apcatb.2019.118268>.
- [29] T.D. Thanh, N.D. Chuong, H. Van Hien, N.H. Kim, J.H. Lee, CuAg@Ag core-shell nanostructure encapsulated by N-Doped graphene as a high-performance catalyst for oxygen reduction reaction, *ACS Appl. Mater. Interfaces* 10 (2018) 4672–4681, <https://doi.org/10.1021/acsami.7b16294>.
- [30] D.C. Nguyen, T.L.L. Doan, S. Prabhakaran, D.H. Kim, N.H. Kim, J.H. Lee, Rational construction of Au@Co₂N_{0.67} nanodots-interpersed 3D interconnected N-graphene hollow sphere network for efficient water splitting and Zn-air battery, *Nano Energy* 89 (2021), 106420, <https://doi.org/10.1016/j.nanoen.2021.106420>.
- [31] Y. Wang, K. Jiang, H. Zhang, T. Zhou, J. Wang, W. Wei, Z. Yang, X. Sun, W.B. Cai, G. Zheng, Bio-inspired leaf-mimicking nanosheet/nanotube heterostructure as a highly efficient oxygen evolution catalyst, *Adv. Sci.* 2 (2015) 1500003, <https://doi.org/10.1002/advs.201500003>.
- [32] S. Chen, L. Ma, S. Wu, S. Wang, Z. Li, A.A. Emmanuel, M.R. Huqe, C. Zhi, J. A. Zapien, Uniform virus-like Co–N–Cs electrocatalyst derived from prussian blue analog for stretchable fiber-shaped Zn–Air batteries, *Adv. Funct. Mater.* 30 (2020) 1908945, <https://doi.org/10.1002/adfm.201908945>.
- [33] R. Gao, L. Liu, Z. Hu, P. Zhang, X. Cao, B. Wang, X. Liu, The role of oxygen vacancies in improving the performance of CoO as a bifunctional cathode catalyst for rechargeable Li–O₂ batteries, *J. Mater. Chem. A* 3 (2015) 17598–17605, <https://doi.org/10.1039/C5TA03885E>.
- [34] Y. Liu, C. Xiao, M. Lyu, Y. Lin, W. Cai, P. Huang, W. Tong, Y. Zou, Y. Xie, Ultrathin Co₃S₄ nanosheets that synergistically engineer spin states and exposed polyhedra that promote water oxidation under neutral conditions, in: *Chemie Angew. (Ed.)*, Int, 54, 2015, pp. 11231–11235, <https://doi.org/10.1002/anie.201505320>.
- [35] Z. Kou, W. Zhang, W. Pei, L. Zheng, S. Zhou, S. Zhang, L. Zhang, J. Wang, A sacrificial Zn strategy enables anchoring of metal single atoms on the exposed surface of holey 2D molybdenum carbide nanosheets for efficient electrocatalysis, *J. Mater. Chem. A* 8 (2020) 3071–3082, <https://doi.org/10.1039/C9TA12838G>.
- [36] D. Wu, W. Zhang, D. Cheng, Facile synthesis of Cu/NiCu electrocatalysts integrating alloy, core-shell, and one-dimensional structures for efficient methanol oxidation reaction, *ACS Appl. Mater. Interfaces* 9 (2017) 19843–19851, <https://doi.org/10.1021/acsami.7b03876>.
- [37] M. Wang, J. Zai, B. Li, Y. Wang, S. Huang, Q. He, X. Qian, Hierarchical Cu_{2–x}Se nanotubes constructed by two-unit-cell-thick nanosheets: room-temperature synthesis and promoted electrocatalytic activity towards polysulfides, *J. Mater. Chem. A* 4 (2016) 4790–4796, <https://doi.org/10.1039/C6TA00184J>.
- [38] S. Yuan, X. Huang, D. Ma, H. Wang, F. Meng, X. Zhang, Engraving copper foil to give large-scale binder-free porous CuO arrays for a high-performance sodium-ion battery anode, *Adv. Mater.* 26 (2014) 2273–2279, <https://doi.org/10.1002/adma.201304469>.
- [39] F. Wu, S. Zhang, B. Xi, Z. Feng, D. Sun, X. Ma, J. Zhang, J. Feng, S. Xiong, Unusual formation of CoO@C “Dandelions” derived from 2D Kagomé MOFs for efficient lithium storage, *Adv. Energy Mater.* 8 (2018) 1703242, <https://doi.org/10.1002/aenm.201703242>.
- [40] T. Ouyang, Y. Ye, C. Wu, K. Xiao, Z. Liu, Heterostructures composed of N-doped carbon nanotubes encapsulating cobalt and β-Mo₂C nanoparticles as bifunctional electrodes for water splitting, *Angew. Chem. Int. Ed.* 58 (2019) 4923–4928, <https://doi.org/10.1002/ange.201814262>.
- [41] W. Zhao, C. Zhang, F. Geng, S. Zhuo, B. Zhang, Nanoporous hollow transition metal chalcogenide nanosheets synthesized via the anion-exchange reaction of metal hydroxides with chalcogenide ions, *ACS Nano* 8 (2014) 10909–10919, <https://doi.org/10.1021/nn504755x>.
- [42] Y.J. Li, J.M. Fan, M.S. Zheng, Q.F. Dong, A novel synergistic composite with multifunctional effects for high-performance Li–S batteries, *Energy Environ. Sci.* 9 (2016) 1998–2004, <https://doi.org/10.1039/C6EE00104A>.
- [43] J. Pu, Z. Shen, J. Zheng, W. Wu, C. Zhu, Q. Zhou, H. Zhang, F. Pan, Multifunctional Co₃S₄@sulfur nanotubes for enhanced lithium-sulfur battery performance, *Nano Energy* 37 (2017) 7–14, <https://doi.org/10.1016/j.nanoen.2017.05.009>.
- [44] S. Hou, Y. Lian, Y. Bai, Q. Zhou, C. Ban, Z. Wang, J. Zhao, H. Zhang, Hollow dodecahedral Co₃S₄@NiO derived from ZIF-67 for supercapacitor, *Electrochim. Acta* 341 (2020), 136053, <https://doi.org/10.1016/j.electacta.2020.136053>.
- [45] K. Dai, N. Zhang, L. Zhang, L. Yin, Y. Zhao, B. Zhang, Self-supported Co/CoO anchored on N-doped carbon composite as bifunctional electrocatalyst for efficient overall water splitting, *Chem. Eng. J.* 414 (2021), 128804, <https://doi.org/10.1016/j.cej.2021.128804>.
- [46] X. Wang, C. Liu, Q. Li, H. Li, J. Xu, X. Chu, L. Zhang, G. Zhao, H. Li, P. Guo, S. Li, X. S. Zhao, 3D heterogeneous Co₃O₄@Co₃S₄ nanoarrays grown on Ni foam as a binder-free electrode for lithium-ion batteries, *ChemElectroChem* 5 (2018) 309–315, <https://doi.org/10.1002/celec.201701050>.
- [47] L. Zhang, L. Wang, H. Lin, Y. Liu, J. Ye, Y. Wen, A. Chen, L. Wang, F. Ni, Z. Zhou, S. Sun, Y. Li, B. Zhang, H. Peng, A lattice-oxygen-involved reaction pathway to boost urea oxidation, *Angew. Chem. Int. Ed.* 58 (2019) 16820–16825, <https://doi.org/10.1002/anie.201909832>.
- [48] W. Yang, Z. Wang, W. Zhang, S. Guo, Electronic-structure tuning of water-splitting nanocatalysts, *Trends Chem.* 1 (2019) 259–271, <https://doi.org/10.1016/j.trechm.2019.03.006>.
- [49] Y. Yan, K. Li, X. Chen, Y. Yang, J.-M. Lee, Heterojunction-assisted Co₃S₄@Co₃O₄ core-shell octahedrons for supercapacitors and both oxygen and carbon dioxide reduction reactions, *Small* 13 (2017) 1701724, <https://doi.org/10.1002/smll.201701724>.
- [50] X. Zhu, J. Dai, L. Li, D. Zhao, Z. Wu, Z. Tang, L.J. Ma, S. Chen, Hierarchical carbon microflowers supported defect-rich Co₃S₄ nanoparticles: An efficient electrocatalyst for water splitting, *Carbon* N. Y 160 (2020) 133–144, <https://doi.org/10.1016/j.carbon.2019.12.072>.
- [51] T. Liu, P. Li, N. Yao, T. Kong, G. Cheng, S. Chen, W. Luo, Self-sacrificial template-directed vapor-phase growth of MoF assemblies and surface vulcanization for efficient water splitting, *Adv. Mater.* 31 (2019) 1806672, <https://doi.org/10.1002/adma.201806672>.
- [52] M. Chauhan, K.P. Reddy, C.S. Gopinath, S. Deka, Copper cobalt sulfide nanosheets realizing a promising electrocatalytic oxygen evolution reaction, *ACS Catal.* 7 (2017) 5871–5879, <https://doi.org/10.1021/acscatal.7b01831>.
- [53] P. Ganesan, A. Sivanantham, S. Shanmugam, Inexpensive electrochemical synthesis of nickel iron sulphides on nickel foam: super active and ultra-durable electrocatalysts for alkaline electrolyte membrane water electrolysis, *J. Mater. Chem. A* 4 (2016) 16394–16402, <https://doi.org/10.1039/C6TA04499A>.
- [54] D.C. Nguyen, D.T. Tran, T.L. Luyen Doan, N.H. Kim, J.H. Lee, Constructing MoP_x@Mn₂P₃ heteronanostructure-supported mesoporous N,P-codoped graphene for boosting oxygen reduction and oxygen evolution reaction, *Chem. Mater.* 31 (2019) 2892–2904, <https://doi.org/10.1021/acs.chemmater.9b00071>.
- [55] X. Guo, M. Li, L. He, S. Geng, F. Tian, Y. Song, W. Yang, Y. Yu, Industrially promising NiCoP nanorod arrays tailored with trace W and Mo atoms for boosting large-current-density overall water splitting, *Nanoscale* 13 (2021) 14179–14185, <https://doi.org/10.1039/D1NR03186D>.
- [56] Y. Jiang, S. Gao, J. Liu, G. Xu, Q. Jia, F. Chen, X. Song, Ti-Mesh supported porous Co₂S nanosheet self-interconnected networks with high oxidation states for efficient hydrogen production via urea electrolysis, *Nanoscale* 12 (2020) 11573–11581, <https://doi.org/10.1039/D0NR02058C>.
- [57] M. Qu, Y. Jiang, M. Yang, S. Liu, Q. Guo, W. Shen, M. Li, R. He, Regulating electron density of NiFe-P nanosheets electrocatalysts by a trifle of Ru for high-efficient overall water splitting, *Appl. Catal. B Environ.* 263 (2020), 118324, <https://doi.org/10.1016/j.apcatb.2019.118324>.
- [58] L. Jiang, N. Yang, C. Yang, X. Zhu, Y. Jiang, X. Shen, C. Li, Q. Sun, Surface wettability engineering: Co₅Ni₃S₂ nanoarray electrode for improving overall water splitting, *Appl. Catal. B Environ.* 269 (2020), 118780, <https://doi.org/10.1016/j.apcatb.2020.118780>.
- [59] P. Colson, A. Schrijnemakers, B. Vertruyen, C. Henrist, R. Cloots, Nanosphere lithography and hydrothermal growth: how to increase the surface area and control reversible wetting properties of ZnO nanowire arrays? *J. Mater. Chem.* 22 (2012) 17086, <https://doi.org/10.1039/c2jm33533f>.
- [60] Y. Liu, W. Chen, S. Wei, W. Gao, TiO₂/ZnO nanocomposite, ZnO/ZnO bi-level nanostructure and ZnO nanorod arrays: microstructure and time-affected wettability change in ambient conditions, *RSC Adv.* 4 (2014) 30658–30665, <https://doi.org/10.1039/C4RA04904G>.
- [61] H. Ang, H.T. Tan, Z.M. Luo, Y. Zhang, Y.Y. Guo, G. Guo, H. Zhang, Q. Yan, Hydrophilic nitrogen and sulfur co-doped molybdenum carbide nanosheets for electrochemical hydrogen evolution, *Small* 11 (2015) 6278–6284, <https://doi.org/10.1002/smll.201502106>.
- [62] J. Song, C. Zhu, B.Z. Xu, S. Fu, M.H. Engelhard, R. Ye, D. Du, S.P. Beckman, Y. Lin, Bimetallic cobalt-based phosphide zeolitic imidazolate framework: CoP_x phase-dependent electrical conductivity and hydrogen atom adsorption energy for efficient overall water splitting, *Adv. Energy Mater.* 7 (2017) 1601555, <https://doi.org/10.1002/aenm.201601555>.
- [63] P. Chen, T. Zhou, M. Zhang, Y. Tong, C. Zhong, N. Zhang, L. Zhang, C. Wu, Y. Xie, 3D nitrogen-anion-decorated nickel sulfides for highly efficient overall water splitting, *Adv. Mater.* 29 (2017) 1701584, <https://doi.org/10.1002/adma.201701584>.
- [64] L. Zhou, M. Shao, J. Li, S. Jiang, M. Wei, X. Duan, Two-dimensional ultrathin arrays of CoP: electronic modulation toward high performance overall water splitting, *Nano Energy* 41 (2017) 583–590, <https://doi.org/10.1016/j.nanoen.2017.10.009>.